

11-11-96
10-19-96
2-11-96
3-11-96

1. Title: The Michelson Stellar Interferometer Error Budget for Triple
Triple-Satellite Configuration
2. Type of Report: A Summary of Research
3. Principal Investigator: Arvind S. Marathay
Graduate Student: Joe Shiefman
4. Period Covered by the Grant: Jan. 30, 1995 - March 31, 1996
5. Institution: The University of Arizona
Optical Sciences Center
Tucson, AZ 85721-0094
6. Grant Number: NAG5-2427



(I) INTRODUCTION

This report presents the results of a study of the instrumentation tolerances for a conventional style Michelson stellar interferometer (MSI). The method used to determine the tolerances was to determine the change, due to the instrument errors, in the measured fringe visibility and phase relative to the ideal values. The ideal values are those values of fringe visibility and phase that would be measured by a perfect MSI and are attributable solely to the object being detected. Once the functional relationship for changes in visibility and phase as a function of various instrument errors is understood it is then possible to set limits on the instrument errors in order to ensure that the measured visibility and phase are different from the ideal values by no more than some specified amount. This was done as part of this study. The limits we obtained are based on a visibility error of no more than 1% and a phase error of no more than 0.063 radians (this comes from 1% of 2π radians). The choice of these 1% limits is supported in the literature.¹

The approach employed in the study involved the use of ASAP (Advanced System Analysis Program) software provided by Breault Research Organization, Inc., in conjunction with parallel analytical calculations. A drawing of the MSI modeled in ASAP is shown in figure 1. The interferometer accepts object radiation into two separate arms each consisting of an outer mirror, an inner mirror, a delay line (made up of two moveable mirrors and two static mirrors), and a 10:1 afocal reduction telescope. The radiation coming out of both arms is incident on a slit plane which is opaque with two openings (slits). One of the two slits is centered directly under one of the two arms of the interferometer and the other slit is centered directly under the other arm. The slit plane is followed immediately by an ideal combining lens which images the radiation in the fringe plane (also referred to subsequently as the detector plane). The ASAP output (i.e. fringes) are shown in figure 2. Figure 2a shows a two dimensional view of the fringes while figure 2b shows a one dimensional slice in x (at $y = 0$) which is representative of a fringe pattern that would be used by ASAP in the measurement of visibility and phase.

The report is divided into the following parts:

- (I) Introduction
- (II) Design of the ASAP programs
- (III) ASAP system verification: procedure and results
- (IV) System tolerance results
- (V) Instrument Error Tolerance Chart
- (VI) Report conclusions
- (VII) Recommendations for further study

(II) DESIGN OF THE ASAP PROGRAMS

In ASAP one generates objects with a specified size, shape, optical properties, and location. Each radiation source is represented as a field with a specified amplitude, phase, size, direction, location, and wavelength. That field is represented by a decomposition into a weighted sum of gaussian beams. Each of the gaussian beams is represented by a base ray and either 4 or 8 (4 if the beam is radially symmetric and 8 if the beam is astigmatic) divergence and waist rays. This concept is demonstrated in figure 3a. The field can propagate by ray tracing the gaussian beams and appropriately altering them due to interactions with the objects (i.e. changing their amplitude, phase, or direction; this also allows for the splitting of beams into more than one beam at optical interfaces). The field (amplitude, phase, and polarization) at any other point in all 3D space can be calculated by ray tracing the rays and summing up the contributions due to all of the gaussian beams. This method is pictured in figure 3b. More complicated sources(i.e. objects) can be modeled as the sum of many sources. All sources must be represented as the sum of gaussian beams with discrete locations, directions, and wavelengths. In stellar interferometry each point on the source gives rise to a plane wave incident on the interometer. Therefore, in our models we describe the source as a collection of plane waves incident on the outer mirrors. Each plane wave is assigned an amplitude, angle of incidence, and wavelength). As such the source must be sampled at a sufficient frequency to ensure that the overlap of the replicates of the coherence function are spread out far enough to be neglected. Figure 4 shows the effect of a spatially undersampled source (an analogous effect occurs in the temporal case).

Using ASAP several programs were generated that model the MSI. They have the flexibility to change the object's size, shape, displacement from the optical axis, sampling frequency, and spectral distribution (i.e. $E(x,y,z,\lambda)$ for each polarization). Additionally, the programs allow for the translation, rotation, change of size, change of shape, and change of the optical properties of any of the MSI components. These programs generate the appropriate fringe patterns from a wide range of source types and allow for the measurement of the fringe visibility and phase as a function of the amount of change of various system parameters.

(III) ASAP SYSTEM VERIFICATION

Right from the beginning of this project it was recognized that verification of an accurate system model was of primary importance since any data generated by an incorrect system model would be at a minimum a waste of time and possibly even misleading (if the error in the model was not recognized). For this reason, this phase of the project was given an extensive effort. Having stated this, due to the complexity of the model, errors were discovered (and corrected) even after this verification phase was completed. Further, it is clear that such a computer model can never be a perfect model

of a complex, real world situation, and as such will need continual correction in the future as the scope of the applications of the model is increased.

In a previous May 30, 1995 report we spelled out the items that we felt would be necessary to check in order to move on to the next phase (determining system tolerances) with an adequate degree of confidence in our model. That list is repeated below:

Verify Model for the Conventional MSI

- A) Compare fringe output for the “plane wave” source to the results from the simpler model
- B) Compare visibility versus baseline output for the “plane wave” source to the results from the simpler model
- C) Verify two dimensional source 2-D fringe results
- D) Check that fringe patterns look correct for various situations
 - 1) Varying slit separation
 - 2) Varying slit width
 - 3) Mirror tilt
 - 4) Fringe visibility for varying source size/ baseline combinations
 - a) source of two points with various angular separations
 - b) source of many points with various angular separations
 - c) source with gaussian flux distribution
 - d) source with a one plus sinc flux distribution
 - e) asymmetric object
 - 5) Fringe visibility due to unequal intensities in the two interferometer arms
- E) Verify that visibility stays constant across the sub-fields in the presence of diffraction fall-off of the fringes
- F) Verify that the visibility falls off correctly across the sub-fields due to a finite spectral bandwidth
- G) Verify that visibility doesn’t change due solely to changes of source flux
- H) Test effect of asymmetrical placement of outer mirrors to establish the presence of the extra phase term predicted by the Van Cittert - Zernike theorem
- I) Verify that moving the source off axis causes the appropriate phase shift
- J) Verify that a symmetrical object gives zero phase at all baselines
- K) Verify that an asymmetrical object gives the correct phase versus baseline output
- L) Verify that effect of delay lines give correct phase shifts

Most of these items we were able to verify by comparing the ASAP output to very straightforward calculations involving primarily the Van-Cittert Zernike theorem, Fourier analysis, and basic interference theory. Several of these items also fall in the category of instrumentation errors and there was accordingly some overlap between the system

verification and instrument tolerance determination. Additionally, two of the items on the verification list were dropped. Item C) (the 2-D source) was dropped primarily because it added much complexity to the ASAP model. This in turn would have resulted in larger programs requiring longer programming times, more difficult and longer debugging times, and longer program run times. It was also felt that there was no shortage of tolerance issues that could be investigated with a 1-D model, and that most of those results had essentially the same conceptual basis as a 2-D model (in the 1-D source each source point radiates a two dimensional plane wave but the plane waves are differentiated by angles that vary only along one axis). Perhaps at some later time the model can be extended to include a 2-D source. Item H) was also dropped when it was determined to be of rather minor interest compared to the many more pertinent issues that existed.

In addition to these items that we had proposed to check, we also verified several items that we had not proposed (some inadvertently). Significant among the additional verification items was the generation of point spread functions (PSF) for each slit independently and for the total system (both slits). We did this for many system configurations (slit sizes, slit separations, wavelengths, etc.). One such example is shown in figure 5. It turned out that examining the PSF proved to be a very valuable tool in understanding the source of visibility and phase errors incurred due to instrumentation errors.

All of the items that we checked were found to agree with the theory to better than 1%. We have included a few examples of the more interesting cases. Figure 6a shows a visibility versus baseline plot for a source with a gaussian shaped radiance distribution. As expected the visibility versus baseline is also gaussian and has the appropriate values. Figure 6b shows the visibility versus baseline for a source with a two point radiance distribution. It shows the correct modulus cosine shape. Figures 7a and 7b show the visibility versus baseline and the phase versus baseline plots for a source with a rectangular radiance distribution. The figures show the expected modulus sinc visibility with the π phase shifts where appropriate. Figures 8a and 8b show the visibility versus baseline and phase versus baseline plots for a source with a triangular radiance distribution. The visibility plot has the appropriate sinc squared shape and the phase is essentially zero (the three different levels in this phase plot are ± 0.003 and 0.000 radians. They reflect the least count digitization of the model. Figures 9a, 9b, 9c, and 9d are 3-dimensional plots where the two variable axes are baseline and OPD (optical path difference) and the vertical (response) axis is visibility. A slice along the line $OPD = 0$ would correspond to the visibility versus baseline plots that were shown in figures 6, 7, and 8. Figure 9a is a plot for a monochromatic source and therefore exhibits no change in visibility with OPD. Figure 9b represents a source of two wavelengths of equal radiance. Figure 9c represents a source with 11 equally spaced, equal radiance source points (a sampled rectangle function). Figure 9d is due to a source with nine source points. Eight of those nine are of equal radiance and spaced equally in wavelength from 1.005 to 1.040 of some nominal wavelength value. The ninth source point is of equal radiance and is located at a value of 1.13 times the nominal wavelength value. This source was created by accident due to a file name that exceeded the maximum DOS file length and was

therefore read in differently than intended. Nonetheless, for this source and the others in figures 9, the visibility versus OPD slices at any of the baseline values were all found to be equal to the temporal Fourier transform of the source spectral radiance multiplied by the spatial visibility value for that baseline (i.e. the spatial Fourier transform of the source spatial radiance function evaluated at that baseline). This is shown in equation form below:

$$\text{Visibility} = [\mathfrak{F}\{I(v)\}_\tau] \times [\mathfrak{F}\{I(x)\}_{B/\lambda_z}] \quad (1)$$

(IV) SYSTEM TOLERANCE RESULTS

In the same May 30, 1995 report as mentioned in the previous section we also spelled out the instrument errors that we intended to investigate. A copy of the listing from that report is shown below.

Test effect of instrument errors on visibility and phase for both MSI models for various source shape and bandwidth combinations

- 1) Mirror tilts
- 2) Diffraction effects
- 3) Unequal intensity transmission between the two interferometer arms
- 4) Unequal optical path lengths in the two arms
- 5) Mirror flatness
- 6) Mirror surface roughness
- 7) Differential dispersion effects in the two arms
- 8) Combinations of the preceding errors to ascertain interaction effects

As the investigation evolved we were able to investigate all but two of the items in the original plan. Additionally, we investigated several items that were not proposed in the original plan. Item 2) Diffraction effects was dropped because we limited our investigations primarily to symmetrical system configurations (i.e. both arms with approximately equal path lengths). For these types of equal path length configurations diffraction effects are not a significant effect.² Differential dispersion (item 7) was not investigated because the complexity involved would have required much time that we decided would be better spent on other issues. The additional items that we investigated were mirror translational errors, slit location errors, object tracking errors, and out of focus errors.

In the balance of this section we address each of the tolerance items one at a time. For each item we present, in part a), our theoretical understanding as to how that type of instrument error should affect the measured fringe visibility. This reasoning is supported by analytical calculations where appropriate. We then present the results that we

obtained from modeling that instrument error in ASAP. This is followed by a discussion of how well the theory and the ASAP model agreed. To the extent that the two differ, we give our opinions as to the sources of those discrepancies.

This procedure is followed, in part b), by a similar treatment indicating how this type of instrument error influences the phase of the fringes. The entire process, parts a) and b), is then repeated for the next instrument error type until all the items are addressed. Finally, a chart is presented that details all of the results obtained for tolerances at the 1% error level.

(IV.1a) Mirror Tilts: Visibility

The first item is mirror tilt. We have identified three possible mechanisms that can lead to an error in measured visibility due to mirror tilt errors. The first occurs in the case where the tilt is severe enough to cause the beam in the arm with the tilted mirror to not entirely fill the slit. When this happens there is a reduction in the visibility by a multiplicative factor of $2\sqrt{I_1 I_2}/(I_1 + I_2)$. This problem is compounded when the tilt is on the outer mirror. In this case the displacement of the beam at the slit for a given tilt angle is greater due to the longer tilted path length and there can be a loss of radiation due to improper aiming of the beam both at the inner mirror and at the slit. Since the slit is not filled on the side with the tilted mirror, the irradiance value on that side will be less than the value from the other side and the multiplicative factor will be less than one (i.e. a drop in the measured visibility). The extent of this effect is related to the system configuration and is particularly sensitive to the length of the afocal reduction telescopes because the tilt angle increases by the reduction ratio inside the telescope leading to an increased displacement per path length inside the reduction telescope (in our system that is a factor of 10x). There is also an additional visibility reduction due to the tilt which causes the point spread function of the slit with the tilted beam to be centered slightly off the optical axis. This is because the visibility is calculated in a small region about the optical axis and the fact that the on axis irradiance of the point spread function which is centered off axis is less than maximum. This effect is in practice usually negligible, since the tilt angles are small and the point spread function for the typically narrow slits is very wide. The effect of visibility falloff as a function of diminished irradiance reaching the detector plane on axis, from the slit with the tilted beam, is demonstrated with ASAP outputs in figures 10, 11, and 12. Figure 10a shows the beams superimposed onto the left and right slits. Figure 10b show the fringes with a visibility of 1.0. In this case the average flux per unit area was about 84.5 in both arms. Figure 11a shows the beams superimposed over the left and right slits for a MSI with the right inner mirror tilted by 0.0004° . It can be seen that the beam in the right arm is tilted slightly up relative to slit. Nonetheless for the tilt value of 0.0004° most of the irradiance gets to the region of interest and there is only about 0.5% drop in visibility (there is a noticeable shifting of the fringes). For the case of 0.0015° of inner mirror tilt as shown in figures 12a and 12b the flux in the visibility calculation region is about 84.5 from the untilted arm and 1.5 from the tilted arm. This accounts for the drop in visibility to about 26%.

A final error in visibility due to mirror tilt errors arises because the amount of phase shift due to mirror tilt is slightly different for each source point. This effect is explained in figures 13, 14, and 15. Figure 13 shows the change in OPD (ΔOPD) due to an inner mirror tilt error for an on-axis source point. In this case the ΔOPD is $2\alpha^2z$. Figure 14 shows the ΔOPD due to an inner mirror tilt error for an off-axis source point with the source angle in the same direction as the mirror tilt (incoming ray above the axis). In this case the ΔOPD is $(2\alpha-2\theta)Z$. Figure 15 shows the ΔOPD due to an inner mirror tilt error for an off-axis source point with the source angle in opposite direction to the mirror tilt (incoming ray below the axis). In this case the ΔOPD is $(2\alpha+2\theta)Z$. Due to the different ΔOPD 's of each source point, the fringe due to each source point will shift by a different amount than the fringes due to the other source points. This in turn will lead to a change in visibility. This effect is not very significant for astronomical applications because it is only significant for cases where the mirror tilt (α) is of significant amount and the angular subtense of the source is of the same order of magnitude as the mirror tilt (i.e. $2\theta \approx \alpha$). In most interesting astronomical cases θ is very small. An example of this third type of mirror tilt effect is demonstrated in ASAP and displayed in figures 16a and 16b. In figure 16a there is no tilt error ($\alpha = 0$) and the measured visibility is 0.004. In figure 16b the inner mirror tilt error is 0.002° and the measured visibility is 0.011. It is interesting to note that due to this differential shifting of the fringes of each of the source points, the visibility for the tilted mirror case actually went up relative to the untilted case. ASAP models all of these effects very accurately (they were checked to better than 0.1%)

(IV.1b) Mirror Tilt: Phase

Whenever one of the interferometer mirrors is tilted it causes the beam reflected off of that mirror to take a different path to the detector plane than it would for the untilted case. In general the length of that path is different for the tilted versus untilted cases. For the measurement of small astronomical objects and significant amounts of mirror tilt, the tilted path is usually longer than the untilted path. Figure 17 demonstrates this concept by calculating the change in path length due to a tilted inner mirror for an on-axis source point. Just as mentioned above in the visibility part, it can be seen from this figure that the most critical part of the system is the afocal reduction telescope because the angle inside the telescope is multiplied by the reduction ratio. The reduction telescope is even more critical in the phase case than in the visibility case. In the visibility case the beam displacement is proportional to the tangent of the tilt angle. For small angles the tangent of the angle is equal to the angle itself. In the phase case, for small angles, the change in path length (as shown in figure 17) is proportional to the square of the tilt angle. In our ASAP model the reduction telescope has a 10:1 reduction ratio which means that the change in OPD per unit length is 100 times greater inside the reduction telescope than it is in the rest of the interferometer. For this reason it would be beneficial to reduce the length of the reduction telescopes. This in turn raises some difficult optical design issues which we have not addressed in this study. This change in path length in one arm of the interferometer leads to a shifting of the fringes when

combined with the beam from the other untilted arm. The amount of this shift of the fringes is proportional to the change in path length in the tilted arm. When examining the effect on off-axis source points the situation is more complex. As shown in figures 14 and 15, the change in path length for an off-axis point is proportional to $(2\alpha^2 - 2\alpha\theta)Z$ for a source point whose angle is in the same direction as the mirror tilt or $(2\alpha^2 + 2\alpha\theta)Z$ for a source point whose angle is in an opposite direction from the mirror tilt (where α is the tilt angle of the mirror and θ is the incoming angle of the off-axis source point). The second term in this expression $(2\alpha\theta)Z$ contains the contribution due to the source point being off-axis. This was the part discussed in the visibility section, that can give rise to a change in visibility due to the fringes from different source points shifting by different amounts. For sources that are symmetrical about the optical axis the $+\theta$ source point shift will be equal and opposite to the shift of the $-\theta$ source point. Therefore, for a symmetrical source the net fringe shift will be the same as for the on-axis point. Even for sources that are not symmetrical about the optical axis, this effect is only significant when both α and θ are relatively large. For these reasons and the fact that it is not significant in astronomical observations we did not investigate the extent of this phase shift in our ASAP model.

Figure 18 shows the $\Delta O P D$ induced if the outer mirror is tilted by an angle α . It is clear from that figure that this case generates a $\Delta O P D$ that is equal to the sum of the $\Delta O P D$ induced by an inner mirror tilted by an angle α plus an additional term equal to $2\alpha^2 X$ (where X is the distance between the outer and inner mirrors).

Plots of phase shift as a function of inner mirror tilt angle, generated by our ASAP model, is shown in figure 19. The phase shifts for each inner mirror are the same magnitude as the phase shifts for the other inner mirror but are opposite in sign, as they should be. Additionally the plots display a parabolic form as predicted by the theory. Nonetheless, it is clear that the plots do not exactly match the theory. Two major discrepancies between the theory and the ASAP plots appear. First, the amount of phase shift for a given tilt value is not symmetrical about the zero tilt line. Secondly, the phase shift values dip slightly into a region representing phase shifts of the opposite sense. Figure 20 shows plots of phase shift as a function of tilt of the left inner mirror for both the calculated values based on our theory and the values generated by the ASAP program. We have not yet determined the source of these problems but suspect that it may be due to either how the ASAP program handles the phase of the field as it propagates through the slit or how it treats the phase as it propagates through the afocal reduction telescopes. We have some ideas as to how to improve this situation and will be trying them in the near future. As it stands now, we can use the current program for rough calculations of phase shifts for tilts on one side of the untilted position only. Figure 21 displays plots for the phase shifts due to tilts of the right outer mirror. Figure 21a is for a 5 meter baseline, 21b is for a 500 meter baseline, and 21c is for a 700 meter baseline. The amount of additional phase shift due to travel between the outer and inner mirrors is exactly twice that which is predicted by our theory. The error is exactly a factor of 2 for all baselines and for all tilt angles. Although there would seem to be a simple cause for this type of error, we have not yet been able to determine its source. In order to resolve these problems in accurately describing the phase shifts due to mirror tilt errors, we have

scheduled a meeting with Alan Greynolds the creator of the ASAP software. It is our feeling that these problems should be solvable.

(IV.2a) and 2b) Diffraction Effects - Not Studied.

(IV.3a) Unequal Irradiance in the Two Arms: Visibility

Unequal intensities in the two arms leads to a straightforward loss of visibility in the form of a multiplicative factor of $2\sqrt{I_1 I_2}/(I_1 + I_2)$. The relative irradiances are measured in the region where the fringe visibility is calculated. Many situations can give rise to unequal intensities at the fringe plane. Several of them arose as the visibility loss mechanisms for other instrument tolerances items. In this category we have already mentioned the case of mirror tilt. We will see this type of visibility loss again when we discuss mirror figure errors. In ASAP we induced this effect by making one of the mirrors less reflective. Figure 22a shows the visibility versus baseline plots from ASAP for an ideal MSI. Figure 22b shows the same for an MSI which is ideal except that one of the inner mirror reflectances was changed from 100% to 25%. Except for this reflectance difference the two plots were for systems observing the same source in exactly the same configuration. The 25% lower irradiance in the one arm leads to the multiplicative factor of 0.8 which we observed in all of our ASAP computations. Additional causes of unequal irradiances that we have not yet studied include unequal arm transmissions, differential polarization effects, and component size errors.

(IV.3b) Unequal Irradiance in the Two Arms: Phase

If the unequal irradiance in the two arms is due to a uniform loss of radiation in one of the arms, there should be no change in the phase of the fringes. This is exactly what we observed in ASAP runs such as the one used in figure 22. If however, the radiation in one arm is attenuated differently for different source points there will in general be a shifting of the fringes. This type of phase shift was not studied.

(IV.4a) Unequal Optical Path Lengths in the Two Arms: Visibility

The visibility for a monochromatic observation should not change due to unequal path lengths. This is what we observed in our ASAP runs.

(IV.4b) Unequal Optical Path Lengths in the Two Arms: Phase

Unequal optical path lengths in the two arms will give rise to a phase shift of the fringes equal in amount to the OPL difference (both measured in wavelengths or fringes). For this reason it is important to keep the optical path lengths of the two arms equal. One source of this inequality we have already discussed in the section on mirror tilt. Other possible sources of this type of error include different amounts of phase shift on reflection off various system components and different distances between components. We did not

model the path length errors due to different phase shifts on reflection but we did model the different distances between components. We did this by making the delay line longer in one arm than in the other. Our delay lines were made up of four 45° mirrors (two stationary and two moveable). The results of some of those runs are presented in figure 23. The plots in figures 23a and 23b are identical even though figure 23a represents no path length difference and figure 23b represents a path length difference of -5.5×10^{-7} meters. The reason for this is that the wavelength of the measured radiation is also 5.5×10^{-7} meters and the fact that there is a 2π ambiguity in the measurement of a phase shift by the ASAP program whenever the phase shift is measured in a single step. The program can track absolute phase shift provided that the large phase shift values are the result of a series of smaller measured steps. In figure 23c and 23d the induced path difference has a magnitude of 2×10^{-7} but in opposite directions. They both show phase shifts of 2.285 radians as they should.

(IV.5a) Mirror Flatness: Visibility

If there are figure errors on the mirrors it can lead to a reduction in the measured visibility. If the mirrors are not flat, but instead have some other surface figure, there will be an induced aberration in the image produced by the arm of the interferometer that contains the deformed mirror. Whether or not this figure error is sufficient to cause a significant visibility error depends on several competing factors. If the beam from the aberrated mirror grossly overfills the slit, the effect of the aberration is minimized. If for instance the mirror has 1 wave of curvature (ρ^2) across its surface (at ρ_{\max}) but the image of the mirror on the slit is 4 times greater than the slit then the maximum curvature across the slit is only $(1/4)^2 = 1/16$ wave at the edge of the slit (at $\rho_{\max}/4$). This reduction of effect, due to the slit being smaller than the image of the mirror, is even greater for higher order terms than for lower order terms. If for instance, the aberration of the mirror was 1 wave of ρ^4 and the mirror image is 4 times greater than the slit then at the edge of the slit the maximum wavefront error is $(1/4)^4 = 1/256$ waves. Therefore this first of the competing factors is that if the image of the aberrated mirror at the slit is much larger than the slit then the aberration is reduced and lower order terms dominate.

Also if the slits are small then the diffraction limited image of each arm of the interferometer will be very wide and this diffraction effect will have a greater effect on the image near the optical axis than will the figure errors (of reasonable amounts) in the mirrors.

Finally, if the slits are of sufficient width so that the diffraction image from each arm is relatively narrow and the effect of the mirror figure error that falls within the bounds of the slit is large enough, then the image of the arm with the mirror figure error will be significantly degraded when compared to the other arm (without the aberrated mirror). In this case much of the on axis irradiance in the aberrated arm image will be shifted to points off axis. As a consequence of this the on-axis irradiance value in the aberrated arm will drop below the value of the on-axis irradiance from the unaberrated arm. When this happens the visibility will drop off by the $2\sqrt{I_1 I_2}/(I_1 + I_2)$ factor that was

discussed before. This theory is oversimplified due to using the on-axis irradiance values when the visibility calculation window in the ASAP model is 40 micrometers wide. We observed this effect in our ASAP model. By placing 1.6 waves of ρ^5 deformation across one of the mirrors and using a 16 mm wide slit we were able to observe the on-axis irradiance in that arm to drop from 1.912×10^6 to 7.555×10^5 . This caused a visibility reduction factor of 0.901. The measure visibility dropped from the ideal value of 0.947 to 0.859 which agrees with $0.947 \times 0.901 = 0.853$ to better than 1%. The point spread functions for the two arms and the measured fringes are shown in figure 24.

(IV.5b) Mirror Flatness: Phase

Because of the deformation of the mirror, the path length for the wavefront on the aberrated side will be increased (or decreased depending on the direction of the deformation) by an amount twice that of the deformation of the mirror. The fringes will get phase shifted by an amount equal to the average of the phase shift across the slit in waves or radians. We have recently developed an ASAP program to model this phase shift. So far we are getting results that contain up to 20% errors in matching the theory. Figure 25 shows the wavefront phase plot (in waves) across the slit in the arm with the deformed mirror along with the corresponding fringe plot for three cases of inner mirror figure error. Figures 25a and 25b show the phase plot and fringes for systems with +1 waves/meter and -1 waves/meter of linear figure error on one of the 0.2 meter diameter inner mirrors. This leads to a maximum phase difference of about 0.15 waves compared with the nominal value of about 0.02 waves. The fringes are shifted by about 0.09 waves which does not exactly match with an average of half the maximum (i.e. $0.15/2 = 0.075$). Probably the average value is higher than 0.075 when one accounts for the strange shape of the phase plots at the edges of the slits. We have not yet had time to determine whether these artifacts are real or some problem with the program. Figure 25c shows the same type of plots for the case of a system with 40 waves/meter² of quadratic figure error across a 0.2 meter diameter inner mirror. This causes a maximum phase error across the slit of about 0.47 waves. This should equate to a $0.47 \times 2/3 \approx 0.31$ waves of average phase difference across the slit. The phase shift from the fringe plot is about 0.25 waves. The discrepancies between the theory and the ASAP results will require attention so that they can be reduced to a more acceptable level. They may be an issue of insufficient beam sampling of the deformed mirror surface.

(IV.6a) Mirror Surface Roughness: visibility

The theory which we employed follows that which we found in the literature^{3,4}. The basis for that theory is as follows. Surface roughness, which is small compared to the wavelength, introduces only phase errors in the wavefront. When the correlation width of the roughness is small compared to the fringe spacing, then the irradiance can be replaced by its statistical average. Assuming a gaussian surface height distribution with a standard deviation of σ there is a reduction in visibility due to the roughness by a multiplicative factor of $\exp[-8\pi^2\sigma^2/\lambda^2]$. We modeled this in ASAP using a gaussian

random surface height distribution with varying values of σ/λ from 0.02 to 0.12 which is shown in figure 26a. Figure 26b is a plot with the same ASAP values as in 26a shown in dashed line and the theoretical values in solid line. The match is very good out to about $\sigma/\lambda = 0.09$, and can be improved to better accuracy through better choice of the program micro-roughness parameter that determines the amount of light scattered out of the specular beam.

(IV.6b) Mirror Surface Roughness: Phase

Since the surface irregularities are small compared to the wavelength (we used $(\sigma/\lambda)_{\text{MAX}} < 0.15$) there are only slight changes in the phase of the wavefront. Additionally, the random variation in surface heights with a zero mean tends to average out to a zero net phase shift. This is what we observed in ASAP.

(IV.7a) and 7b) Differential Dispersion in the Two Arms - for the reasons stated in the beginning of this section, we did not study this effect.

(IV.8a) and 8b) Combinations of Errors: Interaction Effects - Covered at the End of This Section

(IV.9a) Mirror Translational Errors: Visibility

If one of the inner mirrors is laterally misplaced such that it is either farther from or closer to the optical axis than the other (correctly placed) inner mirror it will not cause a change in the visibility unless the misplacement is enough to cause less radiation to pass through the slit. This is a very manageable tolerance. If one of the outer mirrors is laterally misplaced it will lead to an error in visibility due to the fact that the actual baseline will be slightly different than the baseline to which the measured visibility is assigned. In fact, if one ignores practical issues such as diffraction effects, dispersion effects, etc., the visibility is only a function of the total outer mirror separation since the coherence function that it is measuring is spatially shift invariant.

(IV.9b) Mirror Translational Errors: Phase

Whenever one of the inner mirrors is laterally misplaced it changes the optical path length in that arm which gives rise to a phase shift of the fringes equal in magnitude to the change in OPL (measured in waves or radians). This concept is diagrammed in figure 27. We were able to accurately model this in ASAP. Figure 28 shows the fringe output for a run where the left inner mirror (negative x side) is moved further to the left (more negative in x) by an amount of 4.0×10^{-8} meters. This displacement to the left, of the left inner mirror, shortens the path length in the left arm by 4.0×10^{-8} meters (= 0.073 waves or 0.46 radians @ $\lambda = 0.55 \times 10^{-6}$ meters). This in turn causes the zero OPD fringe to shift to the right by $\Delta x = 0.57 \mu\text{m}$ (also 0.073 waves or 0.46 radians of fringe). Note

that as we indicated in part 9a, the visibility is unchanged from its ideal value due solely to the source angular subtense, the wavelength of the radiation, and the baseline.

(IV.10a) Slit Location Errors: Visibility

When one of the slits is misplaced laterally from its correct position there is no change in visibility unless it is misplaced by enough to cause the beam to not fill the entire slit. There is a small shift in the fringe frequency by an amount equal to $\delta/2\lambda z$ (where δ is the amount of the displacement, λ is the radiation wavelength, and z is the perpendicular distance from the slit plane to the fringe plane. Both the visibility stationarity and the fringe frequency change were observed in the ASAP model.

(IV.10b) Slit Location Errors: Phase

The lateral misplacement of one of the slits has no effect on the fringe phase since the ideal lens causes all collimated beams to have the same OPL to focal point on axis.

(IV.11a) Object Tracking Errors: Visibility

An object tracking error causes the object being observed to be displaced off from the system optical axis. Making use of the Fourier relationship between the source brightness and the spatial coherence function (Van Cittert - Zernike theorem) and the shift theorem of Fourier analysis indicates that this shift of the object off from the optical axis induces a phase shift but no change in the modulus of the coherence function. Therefore, there should be no change in the visibility due to this type of error. This is what we observed in our ASAP programs.

(IV.11b) Object Tracking Errors: Phase

As indicated above in the visibility section, there is an induced phase shift due to a tracking error. The argument of this phase shift term is $2\pi\alpha B/\lambda$ (where α is the angular displacement of the source off from the optical axis, B is the baseline of the MSI, and λ is the wavelength value used for the measurement). Therefore, the phase shift increases by an additional 2π amount every time the quantity $\alpha B/\lambda$ increases by one. This amount of phase shift was obtained in all of our ASAP trials with tracking errors. ASAP plots of phase as a function of baseline for equal and opposite amounts of tracking error are shown in figure 29. In figure 29a the source displacement error is 9.82×10^{-9} radians (2.03 milli arc seconds) to the left of the optical axis and $\lambda = 0.55 \times 10^{-6}$ meters. In figure 29b the source is displaced to the right of the optical axis. Note that both plots show the appropriate π phase discontinuity where the sinc-shaped coherence function goes through a zero.

(IV.12a) Out of Focus Errors: Visibility

When the detector is located in a plane other than the plane of best diffraction focus, the point spread functions of the individual slits do not lie on the optical axis but instead are located symmetrically on either side of the optical axis. Whether a given slit is on the left or right side of the optical axis depends on whether the detector plane is in front of or behind best focus. The location of the zero OPD fringe due to each of the source points is a function of the two path lengths from that source point through the two arms to the detector plane. Therefore, they are essentially unaffected by this out of focus situation. Also, even though the images formed by the two slits do not overlap each other on the optical axis, the offset from the optical axis by one of the slit images is equal in magnitude and opposite in direction to the offset of the other image. Therefore: (1) the locations (phases) of the fringes, due to each of the source points, are unchanged and (2) the irradiance values from both arms, in a small region around the optical axis where the visibility is calculated, are reduced but equal to each other. Therefore, the visibility remains unchanged. There is a problem that can arise if this defocus is large enough to cause a significant irradiance fall-off. This is because in most cases of interest the signal to noise ratio is critical in determining how well the visibility can be measured. Because of this, a large drop in irradiance (i.e. signal) is a problem, even though it does not change the signal visibility. Figure 30 show ASAP plots of this situation. Figure 30a is a plot with a 20 mm wide window which displays the two slit images for a detector plane 0.25 meters in front of best focus for a system where the focal length is 10 meters (the fringes are not completely resolved due to a plot resolution issue but are correct within the image data). Figure 30b shows a plot of the same image data which is only 40 μm wide. Note that the visibility value is unchanged, relative to the in focus value shown in figure 30c, but the image plane irradiance is reduced from a maximum irradiance of 900 (for the in focus case) to a value of 2.5.

(IV.12b) Out of Focus Errors: Phase

Due to the same reasons given above in the visibility part there is also no phase shift for the out of focus case. This can be seen to be modeled correctly in ASAP also in figure 30.

(IV.13a) Combinations of Errors (Interaction Effects): Visibility

We have just begun to generate ASAP runs with multiple instrumentation errors. Early results include a run where there was mirror tilt, mirror lateral placement error, and surface figure error (all on the same inner mirror). Runs were also made where the three errors were induced one at a time. It is interesting to note that the visibility of the combination run (figure 31a) was 0.995 (the error-free visibility is 0.999) while the visibility of the run with only surface figure error was 0.948 (figure 31b). This suggests that somehow the addition of the other two instrument errors diminished the reduction of visibility effect due to the surface error. We have not yet had a chance to consider why this might happen.

(IV.13b) Combinations of Errors (Interaction Effects): Phase

We looked at the phase effects for the same run referred to above in the visibility portion where there was mirror tilt, mirror lateral placement error, and surface figure error (all on the same inner mirror). The total phase shift was -1.1883 radians (figure 31a). Runs were also made where each of the three errors were induced one at a time (figures 31b, 31c, and 31d.. The sum of the three phase shifts due to the one at a time runs was -1.1212. In this case the phase shift due to the three errors in combination was 6% greater than the sum of the one at a time runs.

(V) Instrument Error Tolerance Chart (1% Error Limits)

INSTRUMENTATION ERROR TYPE	VISIBILITY (1%) ERROR	PHASE (1% OF WAVE ERROR)
1. MIRROR TILT	INNER MIRROR $\pm 0.0005^\circ$	INNER MIRROR $\pm 0.00016^\circ$ OUTER MIRROR (BASELINE DEPENDENT) BASELINE=100m: $\pm 0.00015^\circ$ =200m: $\pm 0.00014^\circ$ =500m: $\pm 0.00012^\circ$
3. UNEQUAL IRRADIANCE BETWEEN TWO ARMS	IRRADIANCE IN ONE ARM = 75% IRRADIANCE OF THE OTHER ARM	NO PHASE EFFECT
4. UNEQUAL OPTICAL PATH LENGTHS IN TWO ARMS	NO VISIBILITY EFFECT	$\lambda \times 0.01 = 5.5 \text{ nm } (@\lambda = 550\text{nm})$
5. MIRROR FLATNESS	COMPLICATED FUNCTION OF AMOUNT AND TYPE OF FIGURE ERROR AND SLIT SIZE	0.01 WAVE AVERAGE PHASE ERROR ACROSS SLIT (WAVEFRONT ERROR TWICE THE SURFACE FIGURE ERROR)
6. MIRROR SURFACE ROUGHNESS	$\sigma/\lambda = 0.011$ σ = STD. DEV OF SURFACE HEIGHT DISTRIBUTION/ λ = WAVELENGTH	NO PHASE EFFECT
9. MIRROR LATERAL PLACEMENT ERRORS	INNER MIRROR: NO VIS. EFFECT OUTER MIRROR: MEASURED VISIBILITY ASSIGNED TO INCORRECT BASELINE	INNER MIRROR: $\lambda \times 0.01 = 5.5 \text{ nm } (@\lambda = 550 \text{ nm})$ OUTER MIRROR: NO PHASE EFFECT
10. LATERAL SLIT LOCATION ERRORS	NO VISIBILITY EFFECT UNLESS ERROR LARGE ENOUGH TO CAUSE IRRADIANCE TO DROP ON ONE SIDE OF SLIT	NO PHASE EFFECT
11. OBJECT TRACKING ERRORS	NO VISIBILITY EFFECT	FUNCTION OF BASELINE $\alpha = 0.01\lambda/B$ (B=BASELINE) $\alpha = (\lambda = .55\mu; B=5\text{m}) = 6.3 \times 10^{-8}$ $\alpha = (\lambda = .55\mu; B=50\text{m}) = 6.3 \times 10^{-9}$ $\alpha = (\lambda = .55\mu; B=500\text{m}) = 6.3 \times 10^{-10}$ (α IN RADIANS)
12. OUT OF FOCUS ERRORS	NO VISIBILITY EFFECT (LARGE ERROR WILL CAUSE DROP IN SIGNAL TO NOISE RATIO)	NO PHASE EFFECT (LARGE ERROR WILL CAUSE DROP IN SIGNAL TO NOISE RATIO)

(VI) Report Conclusions

We were able to successfully model the Michelson stellar interferometer (MSI) using ASAP software. Most of the instrument errors are accurately modeled. The few remaining problems (primarily mirror tilt phase errors) should be corrected in the near future. Although issues such as mirror tilt and surface roughness are significant issues in measuring visibility, for the most part the visibility tolerances were quite easily attainable (see instrument error tolerance chart). The tolerances to ensure correct phase measurement are quite stringent. As seen from the tolerance chart, in order to obtain less than 1% of 2π radians error requires mirror tilt angles correct to within a few milliradians, optical path length differences between the two arms of less than 5.5 nanometers, inner mirror placement accuracy of 5.5 nanometers, and object tracking accuracy of better than 1 nanoradian (about 0.2 milliarcsecond).

(VII) Recommendations for Further Study

Clearly, the possible system instrumentation errors that could be modeled is unlimited. Probably the most important future work that could be done would be in the category of combination effects. The parameters of each instrument error for various combinations of instrument errors can be changed and computer results can be generated relatively rapidly. Since an interaction between several instrument errors might not be obvious and a theoretical understanding of that interaction might be complex, it makes sense to use a computer program as a rapid means to search for and identify interaction effect candidates for study. Once an interaction effect is identified via the program, a theoretical understanding of that effect could be attained subsequently. The ability to study instrumentation errors in combination is very important because if there is a coupling or interdependence between several instrumentation errors they will not be discovered by examining one error type at a time.

Other interesting errors that could be studied include: (1) differential dispersion effects, (2) diffraction effects, (3) optical design for real reduction telescope, (4) polarization effects, (5) tilt of reduction telescope (6) scattering due to various causes (we have started to look into this).

A modified version of this program could be used to study real existing stellar interferometers or new concepts such as the three satellite configuration.

References

1. J. Davis, 1979, in: *High Angular Resolution Stellar Interferometry* (I.A.U. Colloquium No. 50), eds. J. Davis and W.J. Tango (astronomy Dept., School of Physics, University of Sydney).
2. W. G. Bagnuolo, Jr., *Diffraction Effects*, Internal Report for CHARA (Center for High Angular Resolution Astronomy, Georgia State University) project
3. C. R. Munneryn and M. Latta, *Rough Surface Interferometry Using a CO₂ Laser Source*, Appl. Opt. **7**, 1858 (1968)
4. O. Kwon, J.C. Wyant, and C.R. Hayslett, *Rough Surface Interferometry at 10.6 μ m*, Appl. Opt. **19**, 1862 (1980)

Publications

1. J. Shiefman, B. Bos, A.S. Marathay, B. Saif, B.D. Seery, *Computer Model for the Michelson Stellar Interferometer (MSI)*, Paper presented at 1995 OSA annual meeting, Symposium on Optical Long Baseline Interferometry

Abstract:

By using a computer model based on the applications language: "Advanced System Analysis Program (ASAP)", (developed by Breault Research, Inc.) the measurement of the visibility and phase of the fringes of the MSI is studied. The computer model is used to establish tolerances and error bounds for a successful operation of the MSI. The types of errors investigated include the influence of the spectral band, tilts and local displacements of all mirrors, and baseline orientation and length. The diffraction effects on the irradiance distribution of fringes is also studied.

Figure Caption List

Figure 1: Oblique drawing of MSI system as modeled in ASAP

Figure 2a: Two-dimensional view of fringes in the detector plane in ASAP model.

Figure 2b: One-dimensional x-slice of fringes in detector plane used to measure visibility and phase.

Figure 3a: Gaussian beam as modeled in ASAP showing base ray, waist rays, and divergence rays.

Figure 3b: Pictorial demonstration of the method used in ASAP to trace field through a system.

Figure 4: Visibility plot in ASAP for a spatially undersampled source.

Figure 5: Typical system point spread function. Shown as one-dimensional x-slice and as two-dimensional view.

Figure 6a: ASAP plot of visibility versus baseline for a source with a gaussian shaped radiance distribution.

Figure 6b: ASAP plot of visibility versus baseline for a source made up of two points of equal radiance.

Figure 7a: ASAP plot of visibility versus baseline for source with rectangular radiance distribution.

Figure 7b: ASAP plot of phase versus baseline for a source with a rectangular radiance distribution.

Figure 8a: ASAP plot of visibility versus baseline for source with triangular radiance distribution.

Figure 8b: ASAP plot of phase versus baseline for source with a triangular radiance distribution.

Figure 9a: Three axis ASAP plot of visibility (on the vertical axis) as a function of baseline and OPD for a monochromatic source with a rectangular shaped spatial radiance distribution.

Figure 9b: Three axis ASAP plot of visibility (on the vertical axis) as a function of baseline and OPD for a source with two spectral wavelengths and a rectangular shaped spatial radiance distribution.

Figure 9c: Three axis ASAP plot of visibility (on the vertical axis) as a function of baseline and OPD for a source with a rectangular shaped spectral distribution and a rectangular shaped spatial radiance distribution.

Figure 9d: Three axis ASAP plot of visibility (on the vertical axis) as a function of baseline and OPD for a source with a rectangle plus displaced delta-function spectral distribution and a rectangular shaped spatial radiance distribution.

Figure 10a: ASAP plots of beams superimposed over left and right slits. All mirrors are in ideal positions.

Figure 10b: ASAP plot of fringes for the ideal (untilted) situation. Shows a visibility of 1.0.

Figure 11a: ASAP plot of beams superimposed over the left and right slits. The position of the beams relative to the right slit shows a slight effect of a right inner mirror tilt of 0.0004° .

Figure 11b: ASAP plot of the fringes for the case of 0.0004° right inner mirror tilt. The visibility has fallen off only slightly to a value of 0.994.

Figure 12a: ASAP plot of beams superimposed over the left and right slits. The position of the beams relative to the right slit shows a large effect of a right inner mirror tilt of 0.0015° .

Figure 12b: ASAP plot of the fringes for the case of 0.0015° right inner mirror tilt. The visibility has fallen off only significantly to a value of 0.267.

Figure 13: Diagram showing the effect of inner mirror tilt on an on-axis source point

Figure 14: Diagram showing the effect of inner mirror tilt on an off-axis source point. Source angle is in the same direction as the mirror tilt.

Figure 15: Diagram showing the effect of inner mirror tilt on an off-axis source point. Source angle is in the opposite direction as the mirror tilt.

Figure 16a: ASAP plot of fringes for a source with a very large angular subtense. System has no mirror tilt error. Visibility is 0.004.

Figure 16b: ASAP plot of fringes for the same source as in 16a but with 0.002° of inner mirror tilt. Visibility is 0.011.

Figure 17: Drawing which illustrates the effect of inner mirror tilt on OPD. The 10x afocal reduction telescope is clearly the most critical region.

Figure 18: Drawing illustrates the change in OPD due to a tilt error of the outer mirror.

Figure 19a: ASAP plot of phase shift as a function of left inner mirror tilt.

Figure 19b: ASAP plot of phase shift as a function of right inner mirror tilt.

Figure 20: Plot of ASAP generated values and theoretical values for phase shift as a function of left inner mirror tilt.

Figure 21a: ASAP plot of phase versus right outer mirror tilt angle at a baseline value of 5 meters.

Figure 21b: ASAP plot of phase versus right outer mirror tilt angle at a baseline of 500 meters.

Figure 21c: ASAP plot of phase versus right outer mirror tilt angle for a baseline of 700 meters.

Figure 22a: ASAP plot of visibility versus baseline for an ideal MSI.

Figure 22b: ASAP plot of visibility versus baseline for same source as in 22a but with the irradiance in one of the arms reduced to 25% that of the other arm. The visibility shows the appropriate 20% drop from the ideal value.

Figure 23a: ASAP plot of phase versus baseline for MSI with equal path lengths in the two arms.

Figure 23b: ASAP plot of phase versus baseline for MSI with one arm having a path length exactly one wavelength greater than the other arm.

Figure 23c: ASAP plot of phase versus baseline for MSI with the left arm having a path length 2×10^{-7} meters shorter than the right arm.

Figure 23d: ASAP plot of phase versus baseline for MSI with the left arm having a path length 2×10^{-7} meters longer than the right arm

Figure 24a: ASAP plot of point spread function for the arm containing the inner mirror with 1.6 waves of ρ^2 surface figure error.

Figure 24b: ASAP plot of point spread function for the arm containing the inner mirror without any surface figure error.

Figure 24c: ASAP plot of fringes for the system shown in 24a and 24b. It shows the appropriate visibility drop.

Figure 25a: ASAP plot of phase versus position across the slit for the arm with the mirror surface figure error. It shows a linear shape with a maximum value of about 0.16 waves at the slit edge. Also a second ASAP plot of fringes for the same system. There is a phase shift of about 0.09 waves which is close to what would be expected.

Figure 25b: ASAP plot of phase versus position across the slit for the arm with the mirror surface figure error. It shows a linear shape with a minimum value of about -0.16 waves at the slit edge. Also an ASAP plot of fringes for the same system. There is a phase shift of about -0.09 waves which is close to what would be expected.

Figure 25c: ASAP plot of phase versus position across the slit for the arm with the mirror surface figure error. It shows a parabolic shape with a maximum value of about 0.47 waves at the slit edge. Also an ASAP plot of fringes for the same system. There is a phase shift of about 0.25 waves which is close to what would be expected.

Figure 26a: ASAP plot of visibility as a function of inner mirror surface roughness.

Figure 26b: Plot of visibility versus inner mirror surface roughness. The same ASAP values as shown in figure 26a are plotted with a dashed line. The values represented by the solid line are the theoretical values.

Figure 27: Drawing which shows the effect of an inner mirror translational error on the location of the zero OPD fringe.

Figure 28: ASAP plot of fringes for an MSI with a left inner mirror located 4×10^{-8} meters to the left of its correct location.

Figure 29a: ASAP plot of phase versus baseline for an MSI with a 9.8×10^{-9} radians tracking error with the source off to the left of the optical axis.

Figure 29b: ASAP plot of phase versus baseline for an MSI with a 9.8×10^{-9} radians tracking error with the source off to the right of the optical axis.

Figure 30a: 20 mm wide ASAP plot of the images from the two slits and a 0.25 meter focus error.

Figure 30b: ASAP plot of same fringes as in 30a but with a $40 \mu\text{m}$ wide window.

Figure 30c: ASAP plot of a similar MSI to 30a and 30b but in correct focus. While it has virtually the same visibility as in 30b, it has a much greater flux value.

Figure 31a: ASAP plot of the fringe closest to the axis for an MSI with one inner mirror containing surface figure error, translational error, and angular tilt error.

Figure 31b: ASAP plot of the fringe closest to the optical axis for an MSI with an inner mirror with only surface figure error.

Figure 31c: ASAP plot of the fringe closest to the optical axis for an MSI with an inner mirror with only translational error.

Figure 31d: ASAP plot of the fringe closest to the optical axis for an MSI with an inner mirror with only angular tilt error.



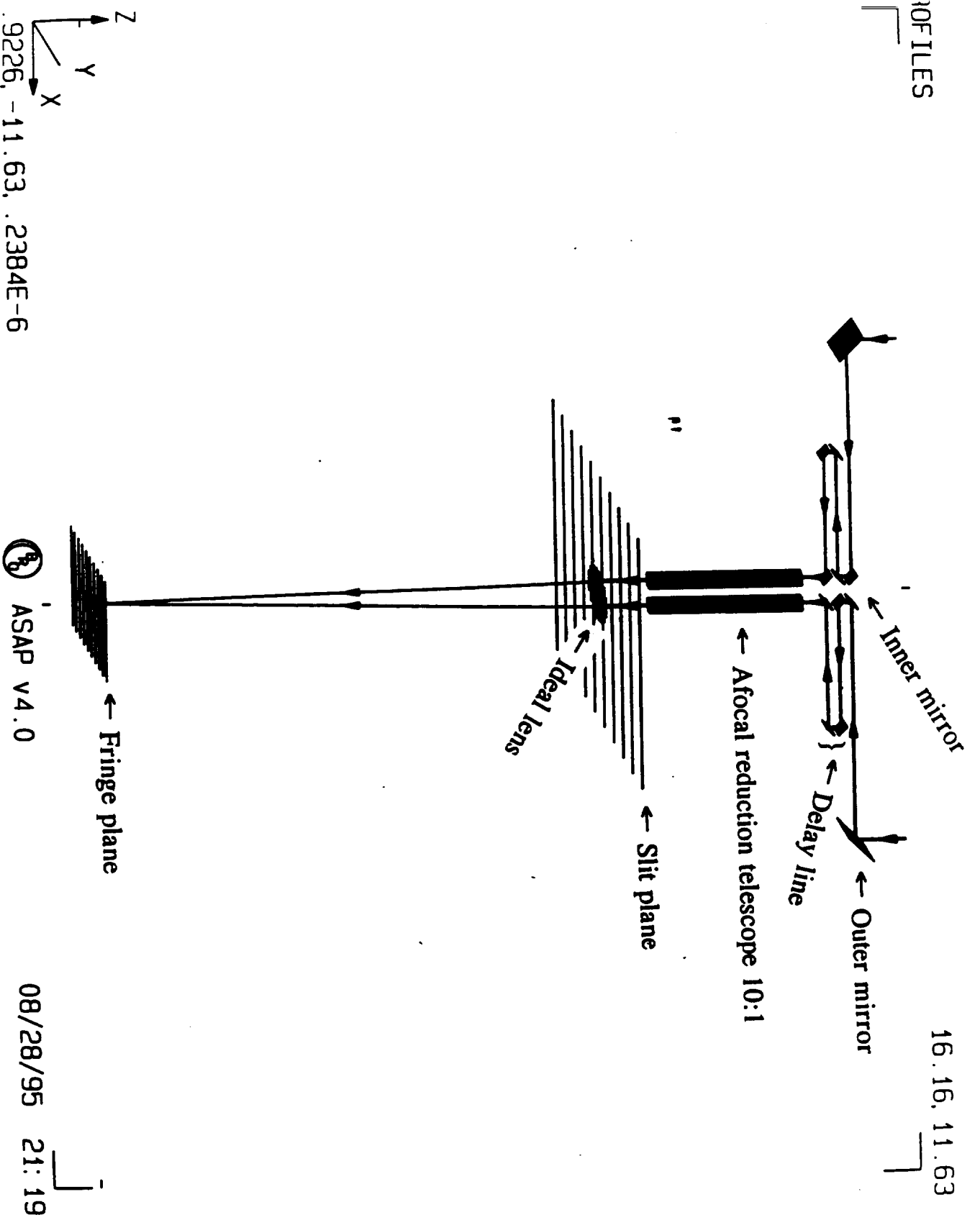


FIGURE 1

SYSTEM OUTPUT - FRINGE PATTERN

FIGURE 2a

Straight line
fringes

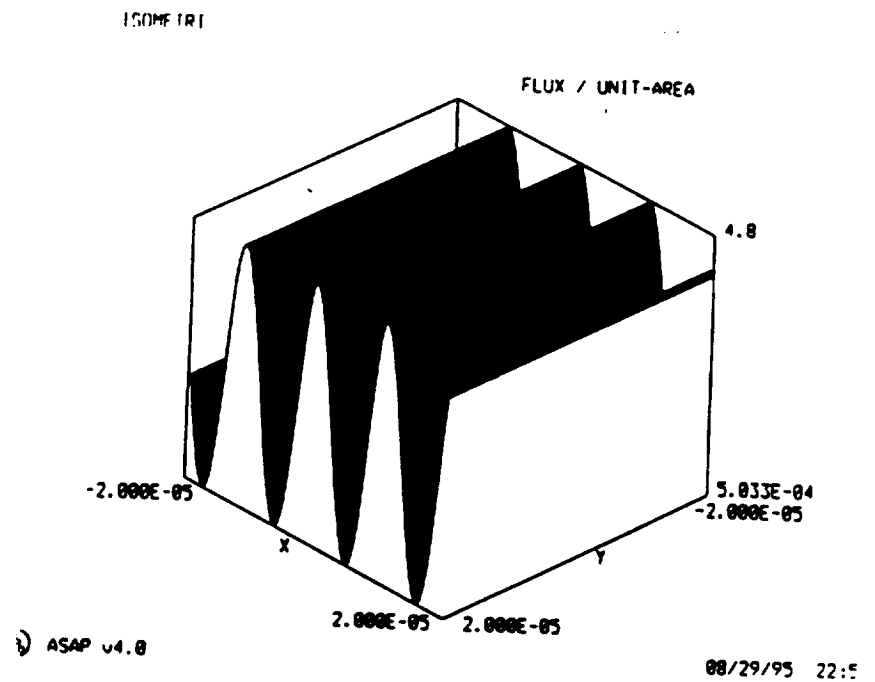
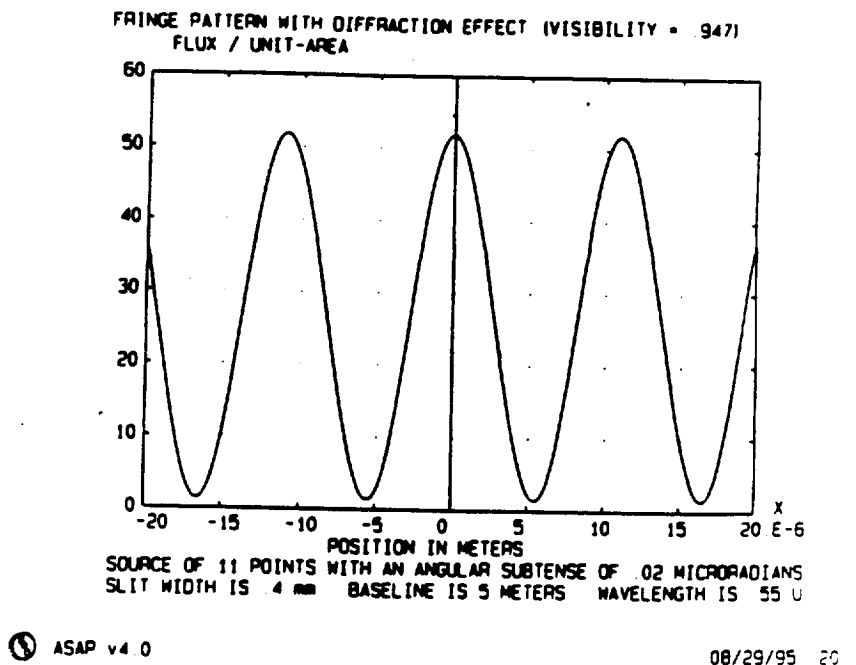


FIGURE 2b

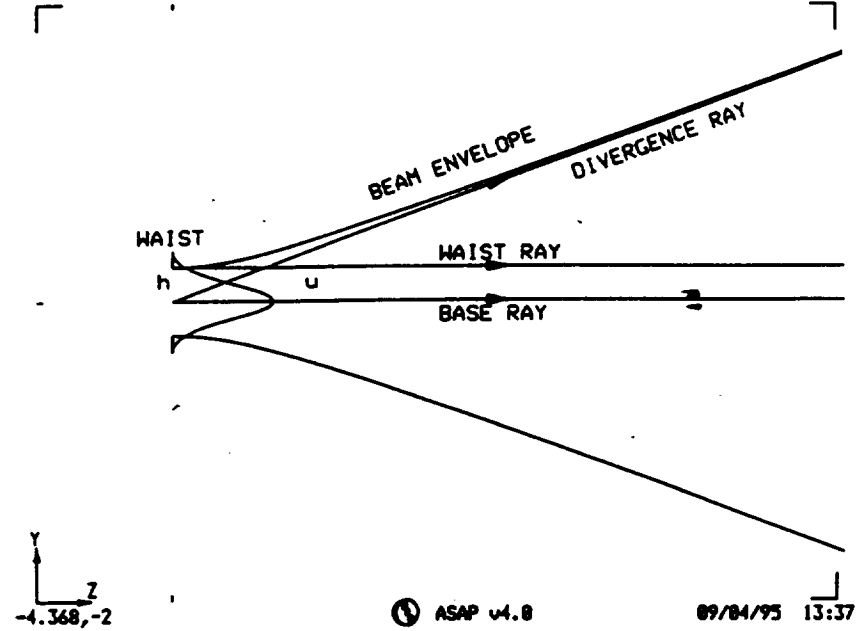
One dimensional
slice at $y = 0$



ASAP GAUSSIAN BEAM PROPAGATION TECHNIQUE

WAIST AND DIVERGENCE RAY REPRESENTATION OF GAUSSIAN BEAM PROPAGATION 4.368,9.9

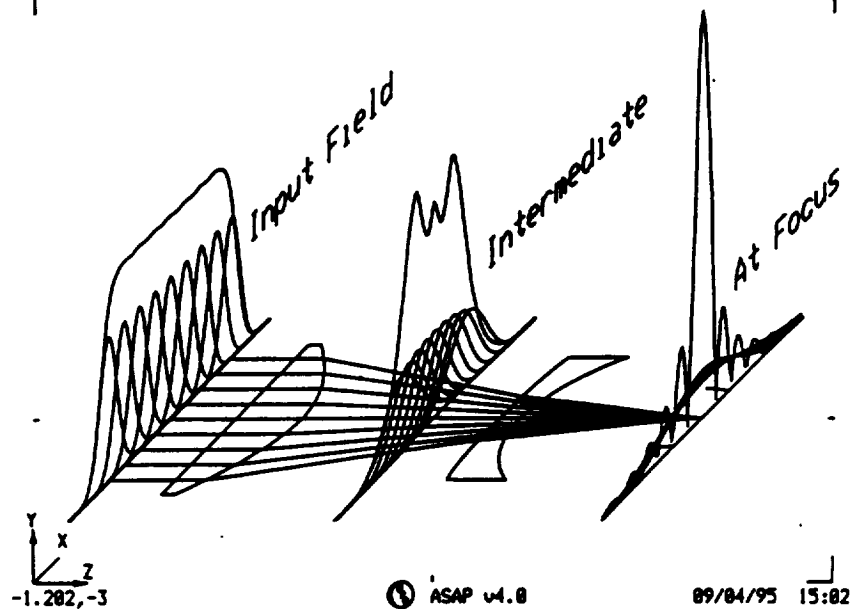
FIGURE 3a



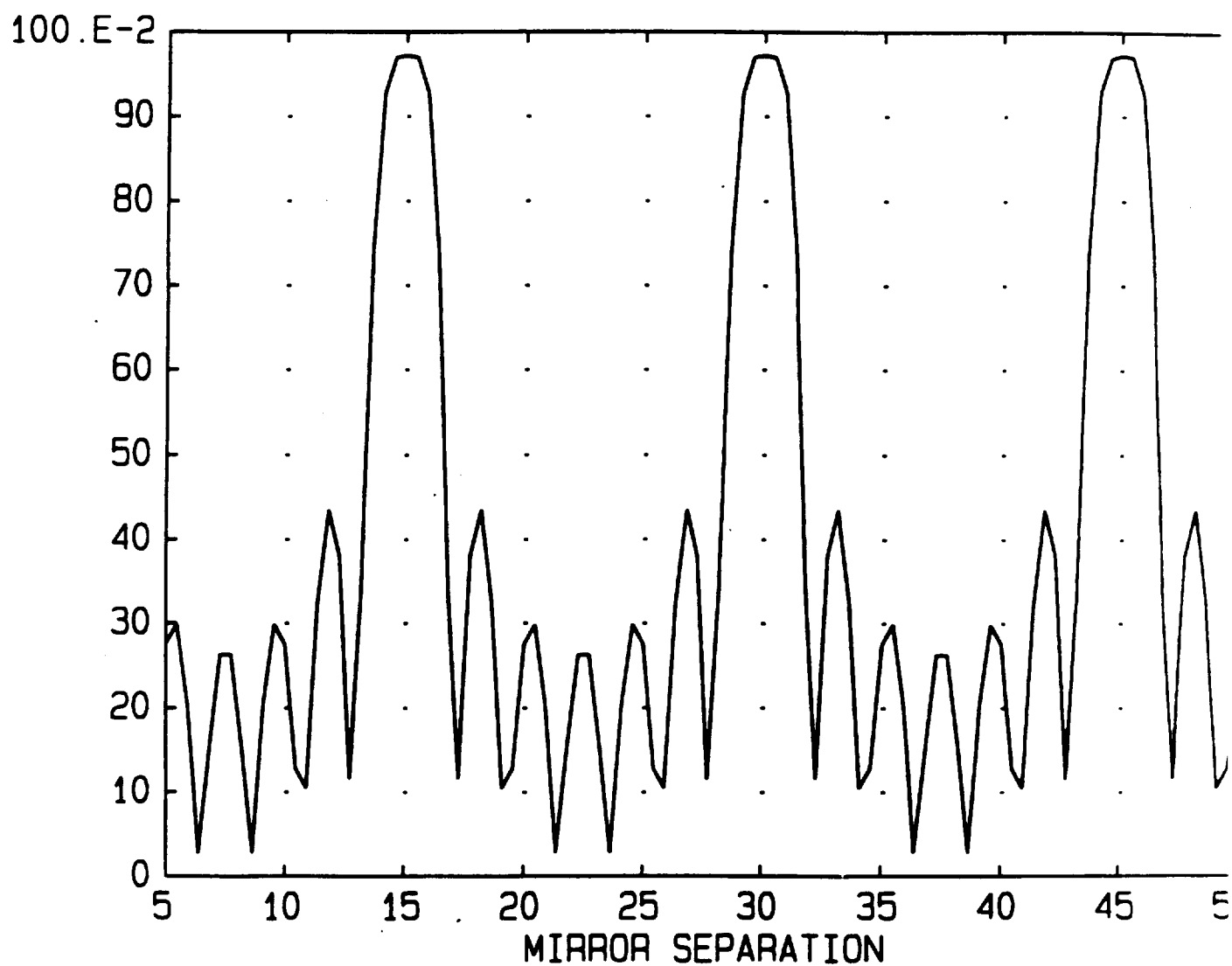
ASAP GAUSSIAN BEAM SUPERPOSITION & PROPAGATION THEORY

3.202,3

FIGURE 3b



VISIBILITY VERSES MIRROR SEPARATION



7 10 UM GAUSSIAN BEAM, LAMBDA=0.55UM, ALPHA=0.05UR
100 POINTS

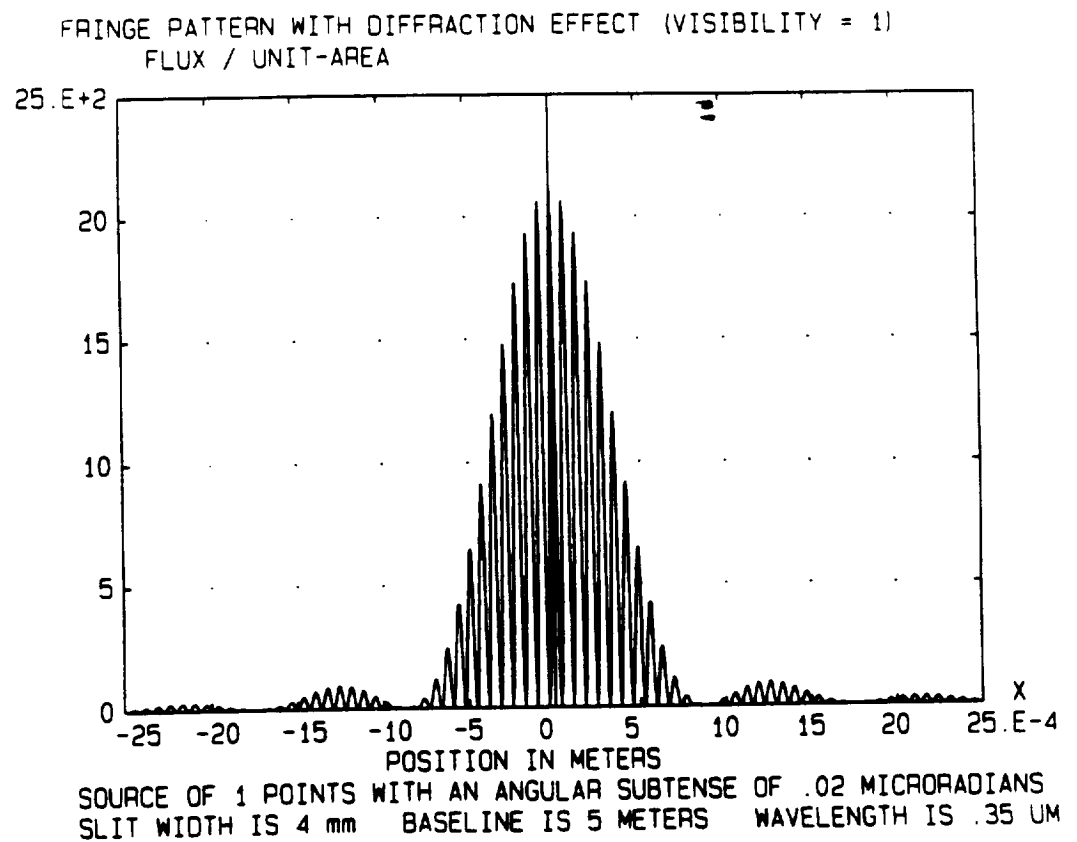
FIGURE 4

SYSTEM MODEL VERIFICATION INSTRUMENT PROPERTIES

METRICS: PSF & Fringe Frequency

TYPICAL SYSTEM POINT SPREAD FUNCTION (PSF)

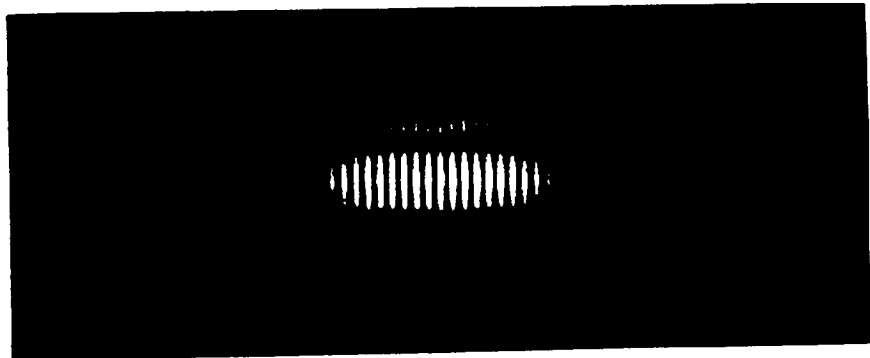
FIGURE 5a



ASAP v4.0

09/04/95 11:57

FIGURE 5b



VISIBILITY VERSUS BASELINE FOR TWO DIFFERENT SOURCES

SOURCE WITH GAUSSIAN SHAPED
RADIANCE DISTRIBUTION

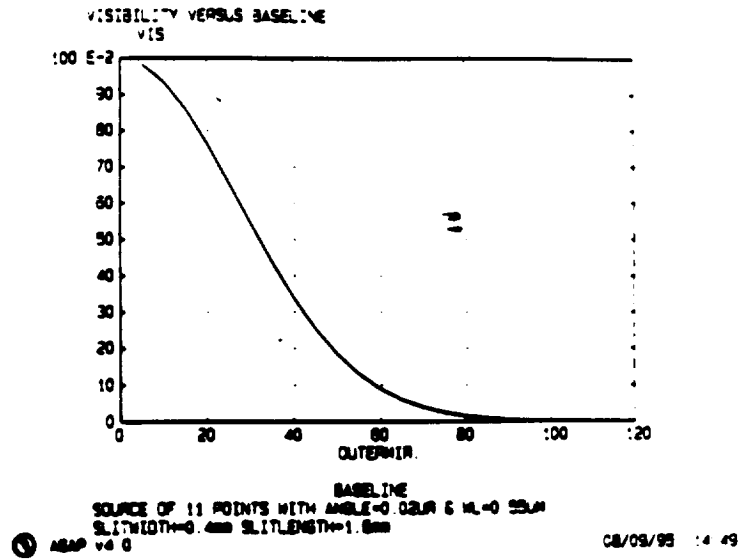


FIGURE 6a

SOURCE OF TWO POINTS WITH
EQUAL RADIANCE

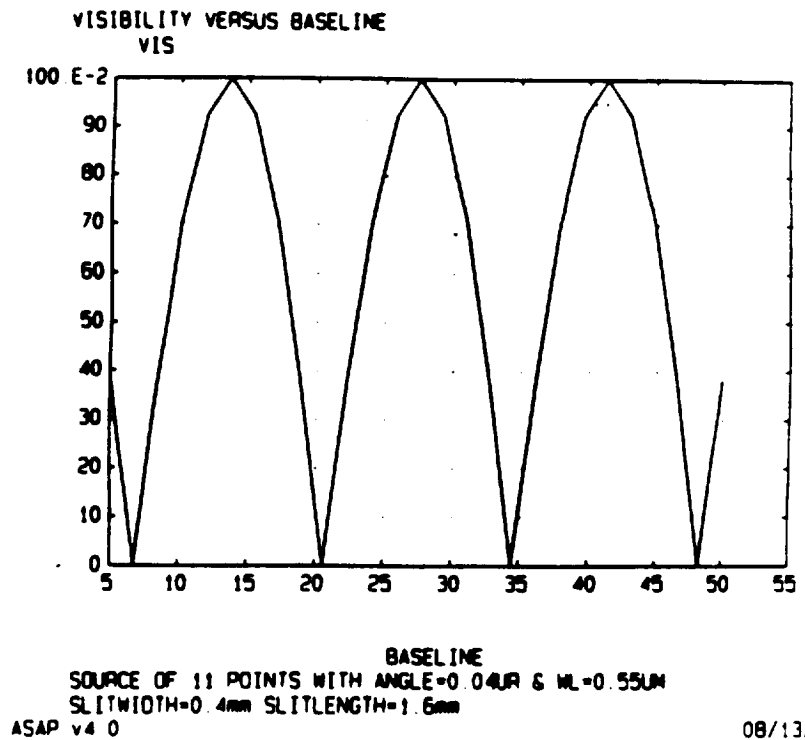


FIGURE 6b

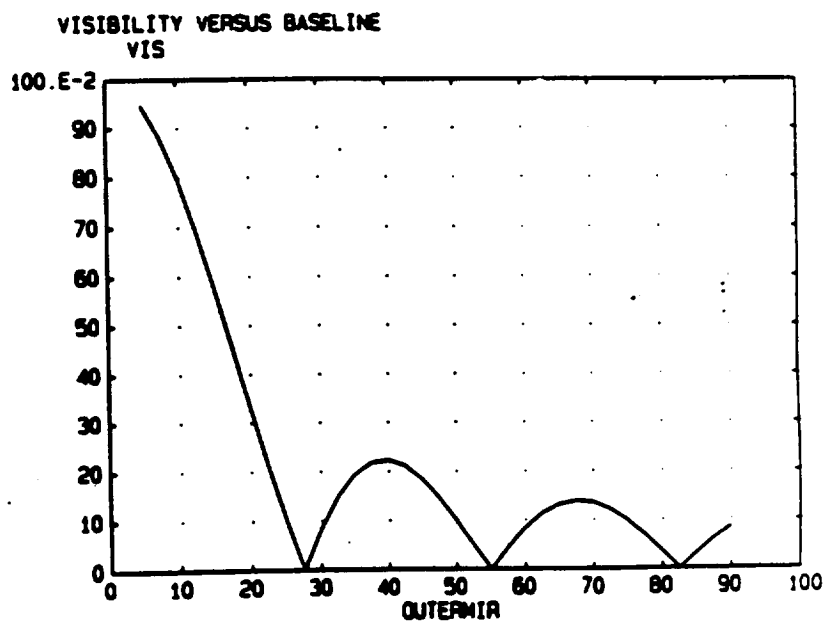
SYSTEM MODEL VERIFICATION SOURCE PROPERTIES

METRICS: VISIBILITY & PHASE

PLOTS FOR SOURCE WITH RECTANGULAR RADIANCE APODIZATION

FIGURE 7a

Visibility vs.
Baseline



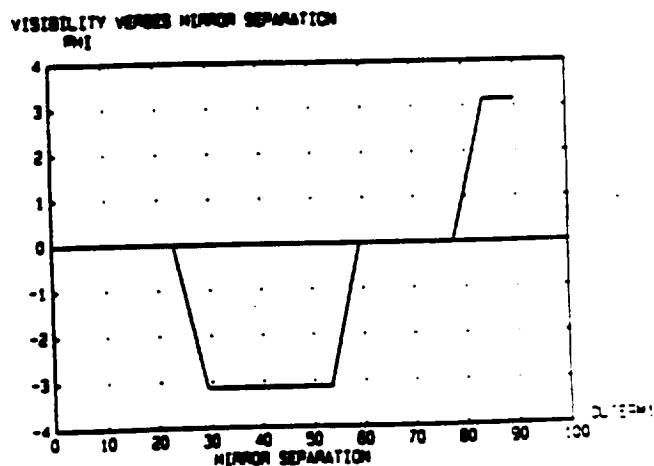
BASELINE
SOURCE OF 11 POINTS WITH ANGLE=0.02UR & WL=0.55UM
SLITWIDTH=0.4mm SLITLENGTH=1.6mm

ASAP v4.0

08/31/95

FIGURE 7b

Phase vs.
Baseline



ASAP v4.0

08/10/95 12:08

SYSTEM MODEL VERIFICATION SOURCE PROPERTIES

METRICS: VISIBILITY & PHASE

PLOTS FOR SOURCE WITH TRIANGULAR RADIANCE APODIZATION

Visibility vs.
Baseline

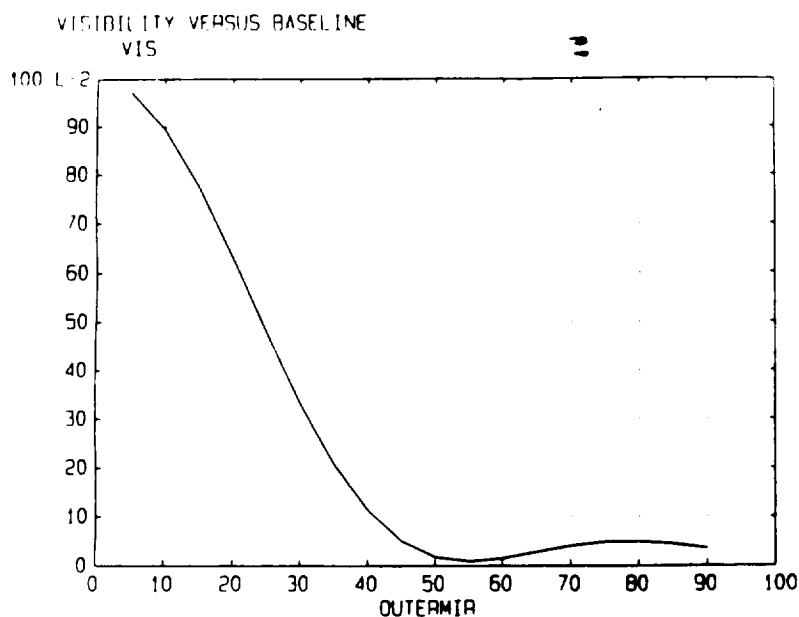


FIGURE 8a

BASELINE
SOURCE OF 11 POINTS WITH ANGLE=0.02UR & WL=0.55UM
SLITWIDTH=0.4mm SLITLENGTH=1.6mm
ASAP v4.0

08/30/95 02:45

Phase vs.
Baseline

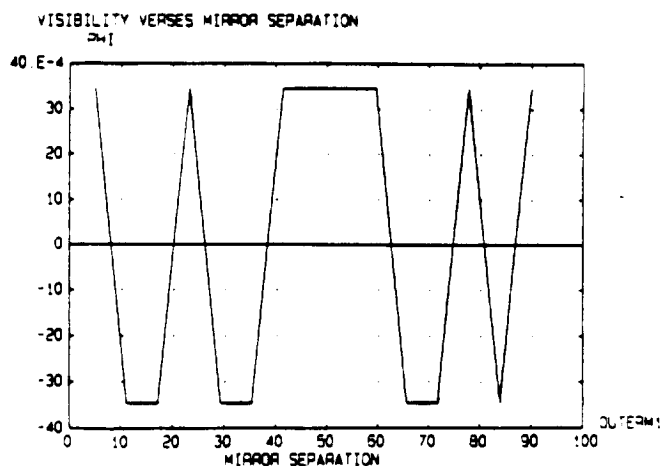


FIGURE 8b

ISOMETRI

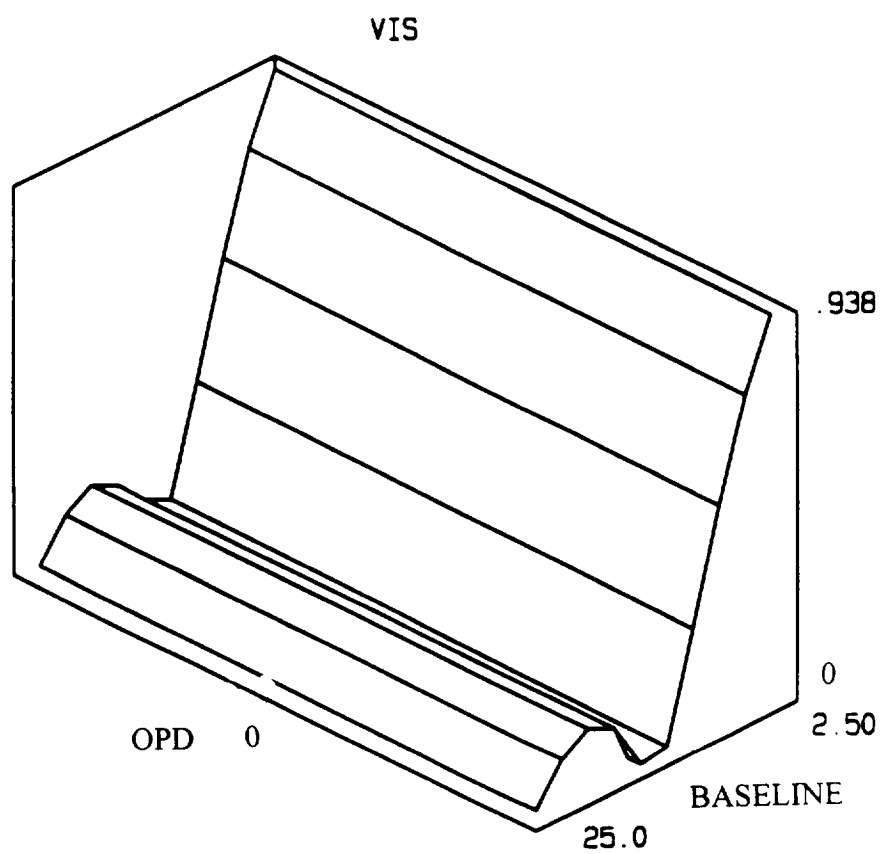


FIGURE 9a

3 POINTS WL=.55 ANG=.02 URAD TOTWS=572UM SUBWS=11UM SM=1.333333333333333M

VISIBILITY

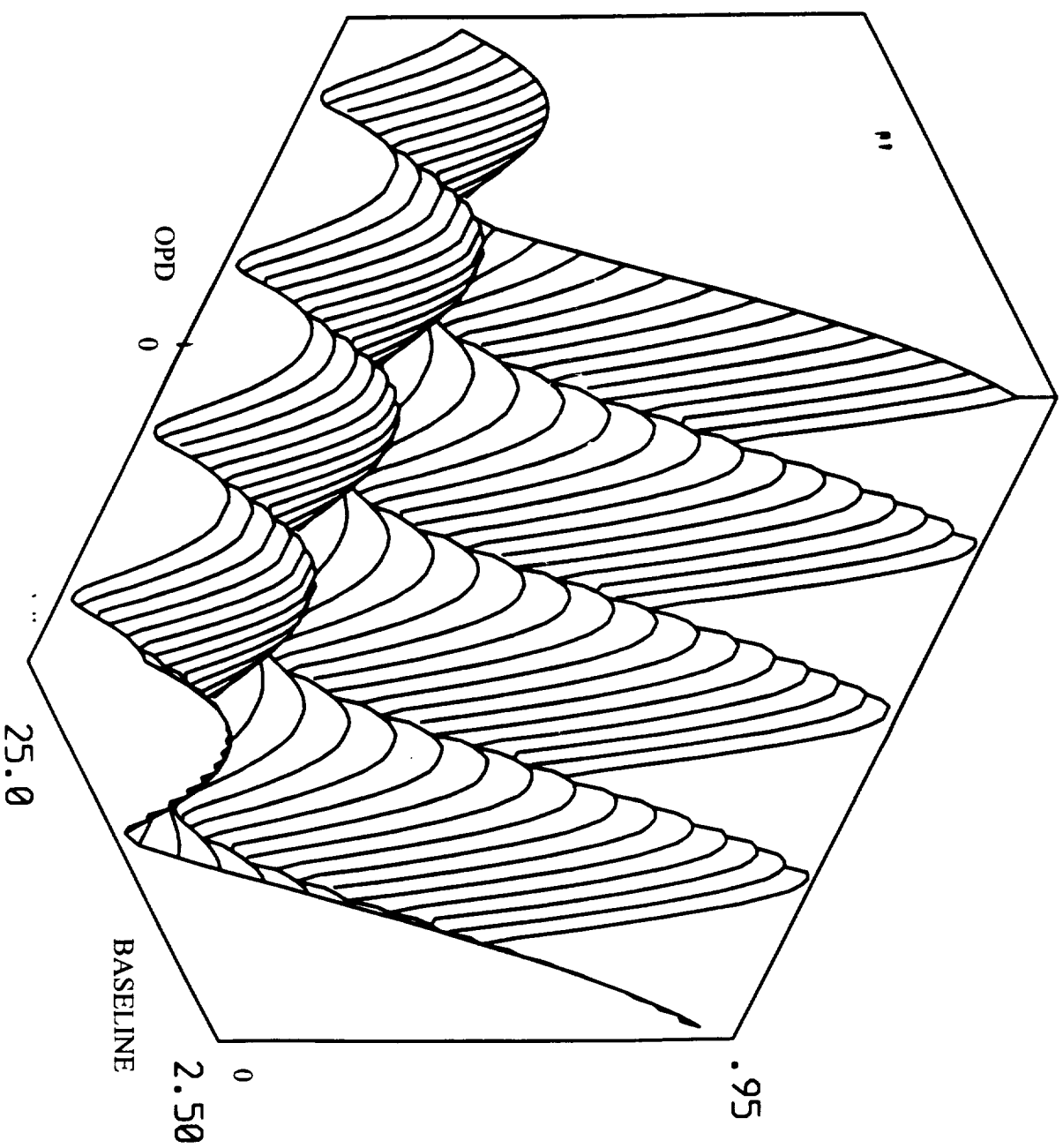


FIGURE 9b

11 POINTS WL=.55 ANG=.02 URAD TOTWS=572UM SUBWS=11UM SW=1.3333333333333333

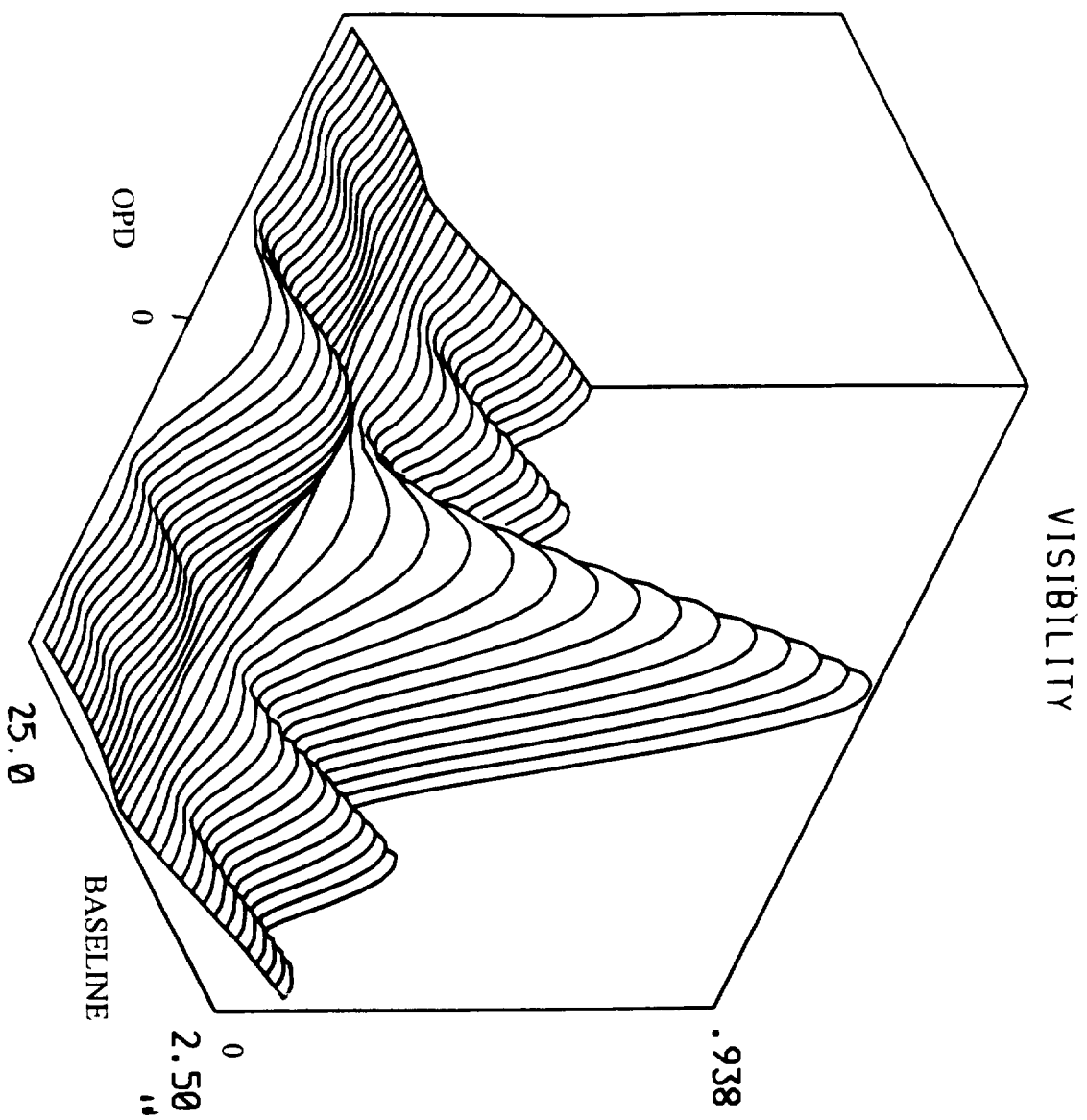


FIGURE 9c

11 POINTS WL=.55 ANG=.02 URAD TOTWS=572UM SUBWS=11UM SW=1.3333333333333333

VISIBILITY

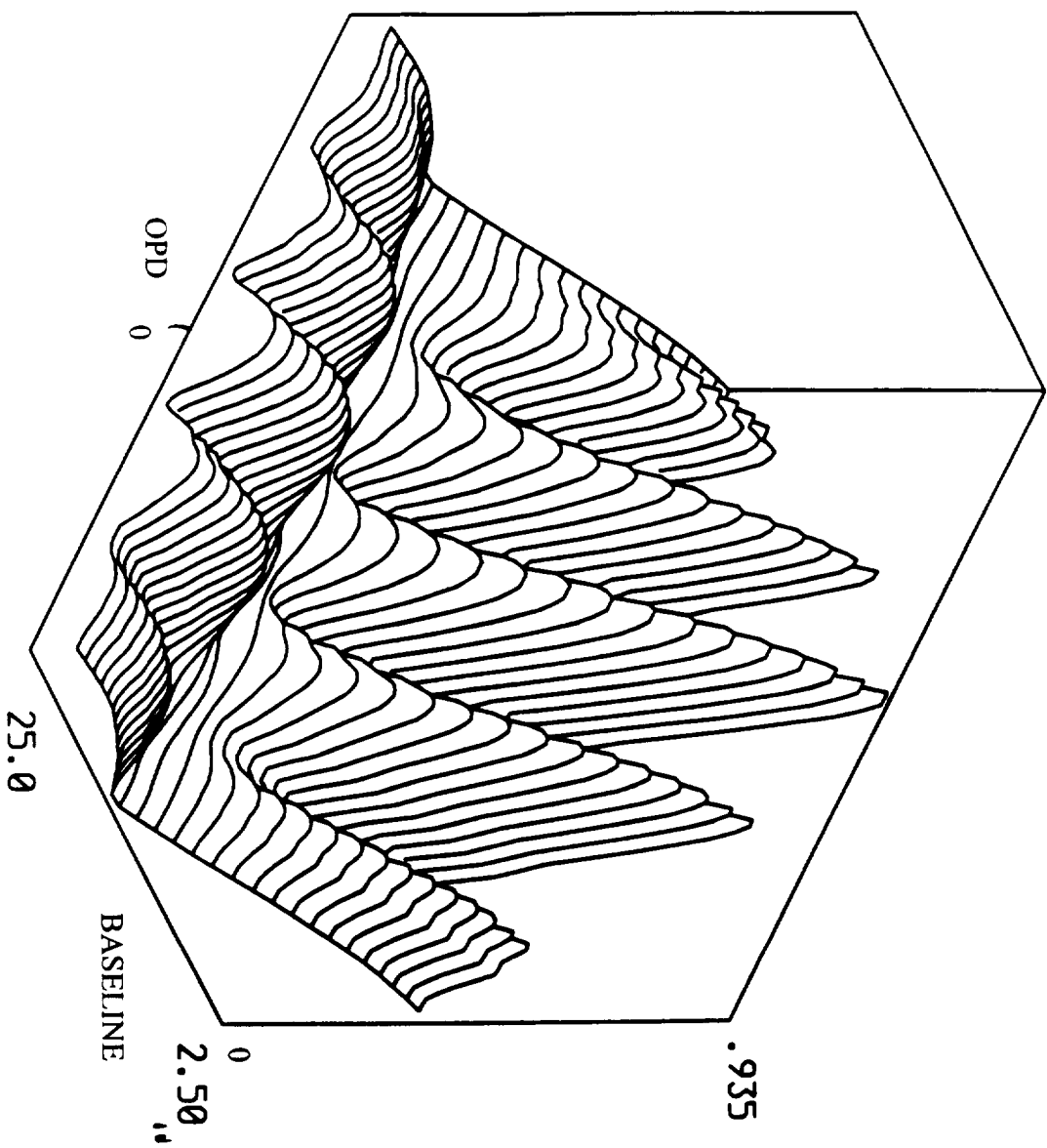


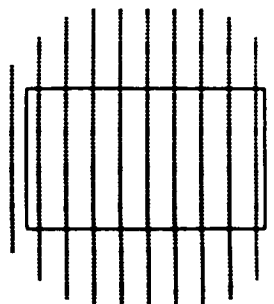
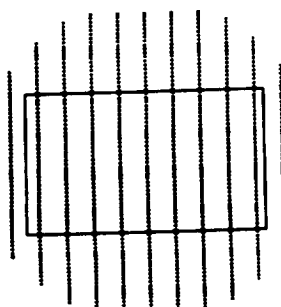
FIGURE 9d

PROFILES

.252..2725E-2

PROFILES

-.252..2725E-2



X
Y
.248,-.2725E-2

ASAP v4.8

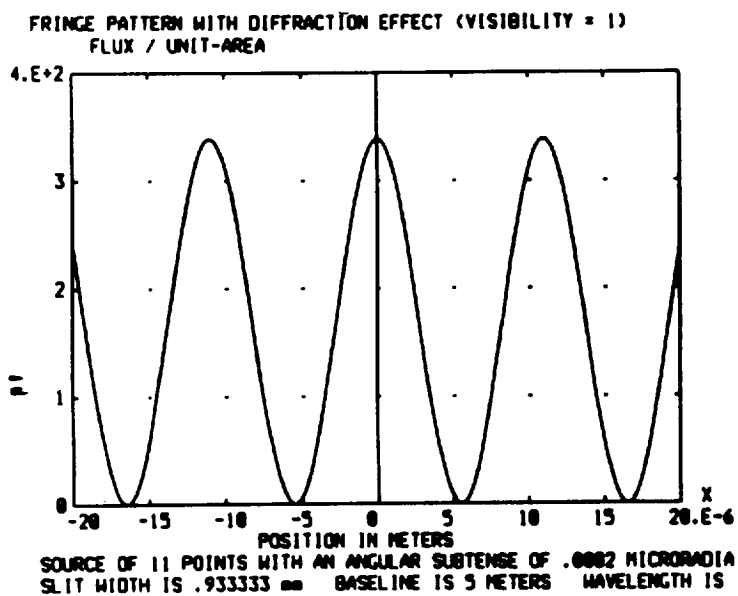
03/14/96 20:21

-X
Y
-.248,-.2725E-2

ASAP v4.8

03/14/96 20:24

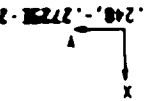
FIGURE 10a



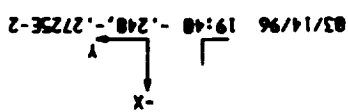
ASAP v4.8

03/14/96 20:26

FIGURE 10b



① ASAP v4.8



① ASAP v4.8

03/14/96 19:42

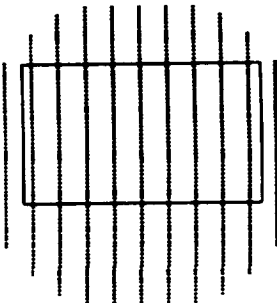
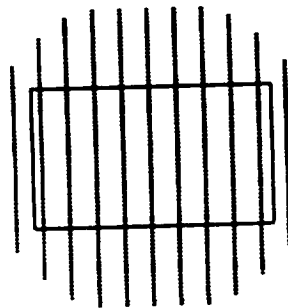
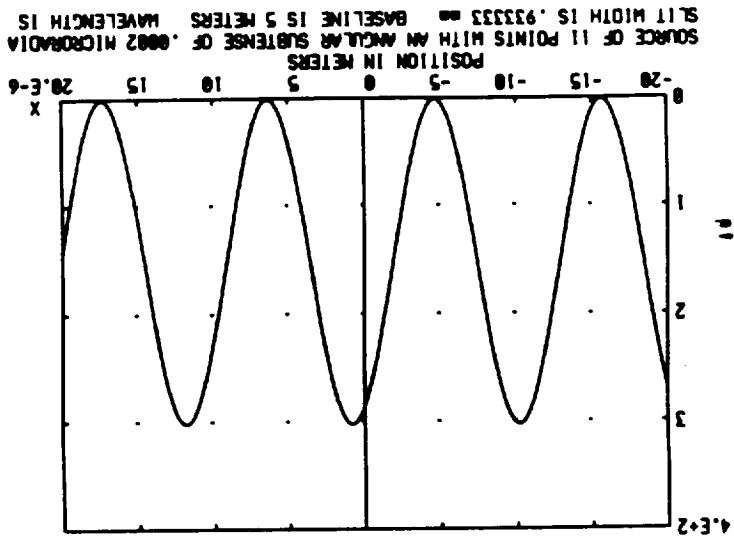


FIGURE 11a

FRINGE PATTERN WITH DIFFRACTION EFFECT (VISIBILITY = .994)
FLUX / UNIT-AREA



SOURCE OF 11 POINTS WITH AN ANGULAR SUBTENSE OF .0002 MICRORADIANS
SLIT WIDTH IS .933333 mm BASELINE IS 5 METERS WAVELENGTH IS

① ASAP v4.8

03/14/96 19:44

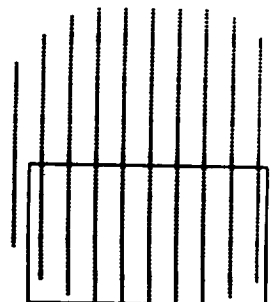
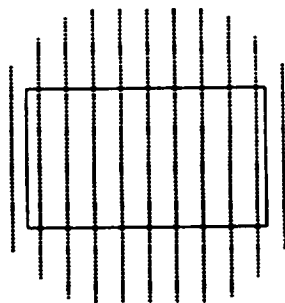
FIGURE 11b

PROFILES

.252..2725E-2

PROFILES

-.252..2725E-2



x
y
.248, -.2725E-2

ASAP v4.0

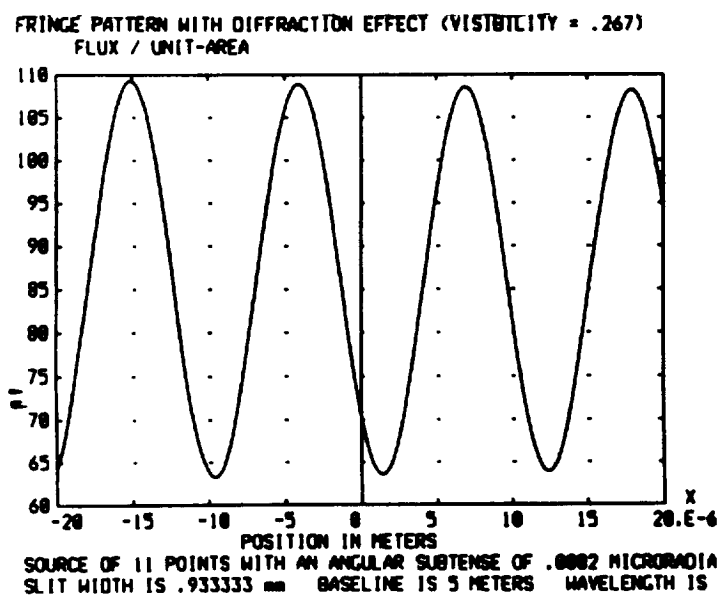
03/14/96 19:48

-x
y
-.248, -.2725E-2

ASAP v4.0

03/14/96 19:51

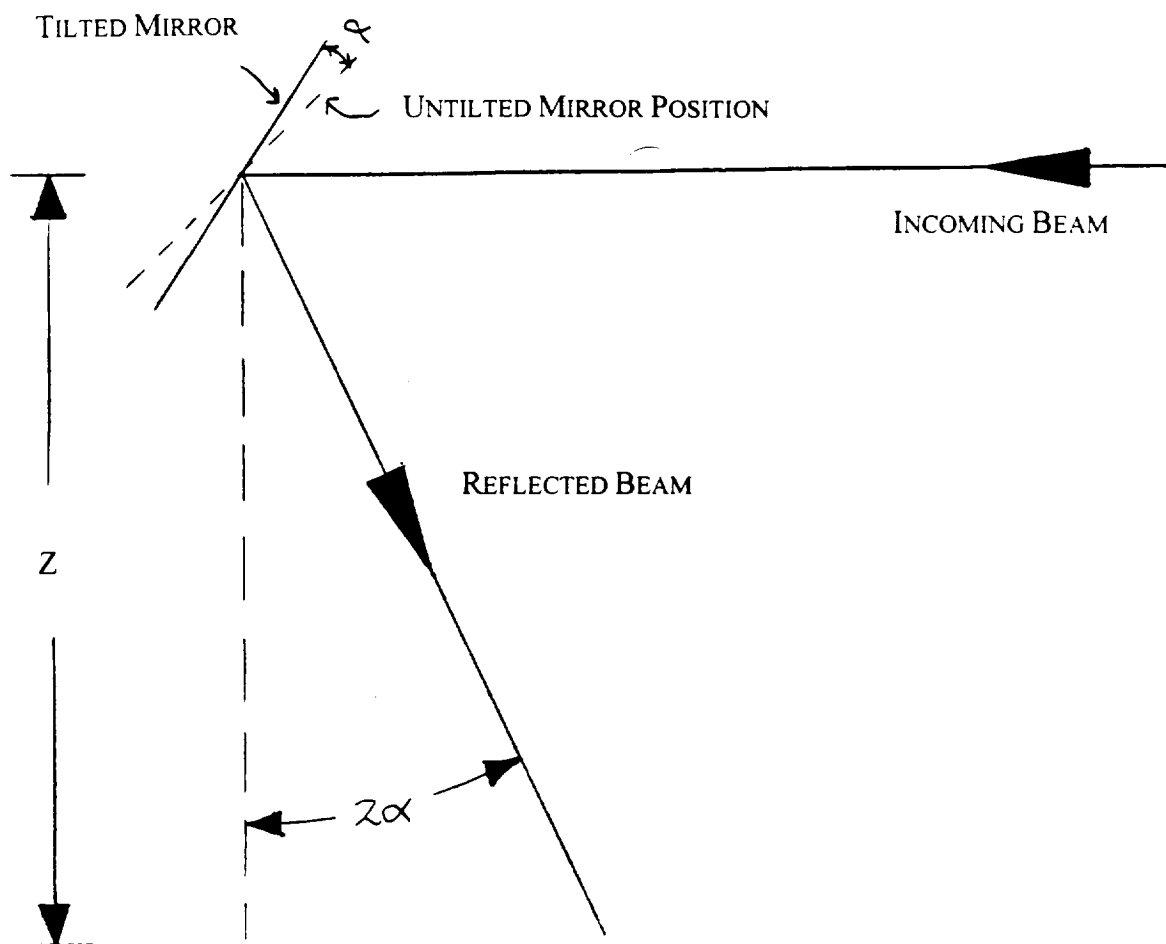
FIGURE 12a



ASAP v4.0

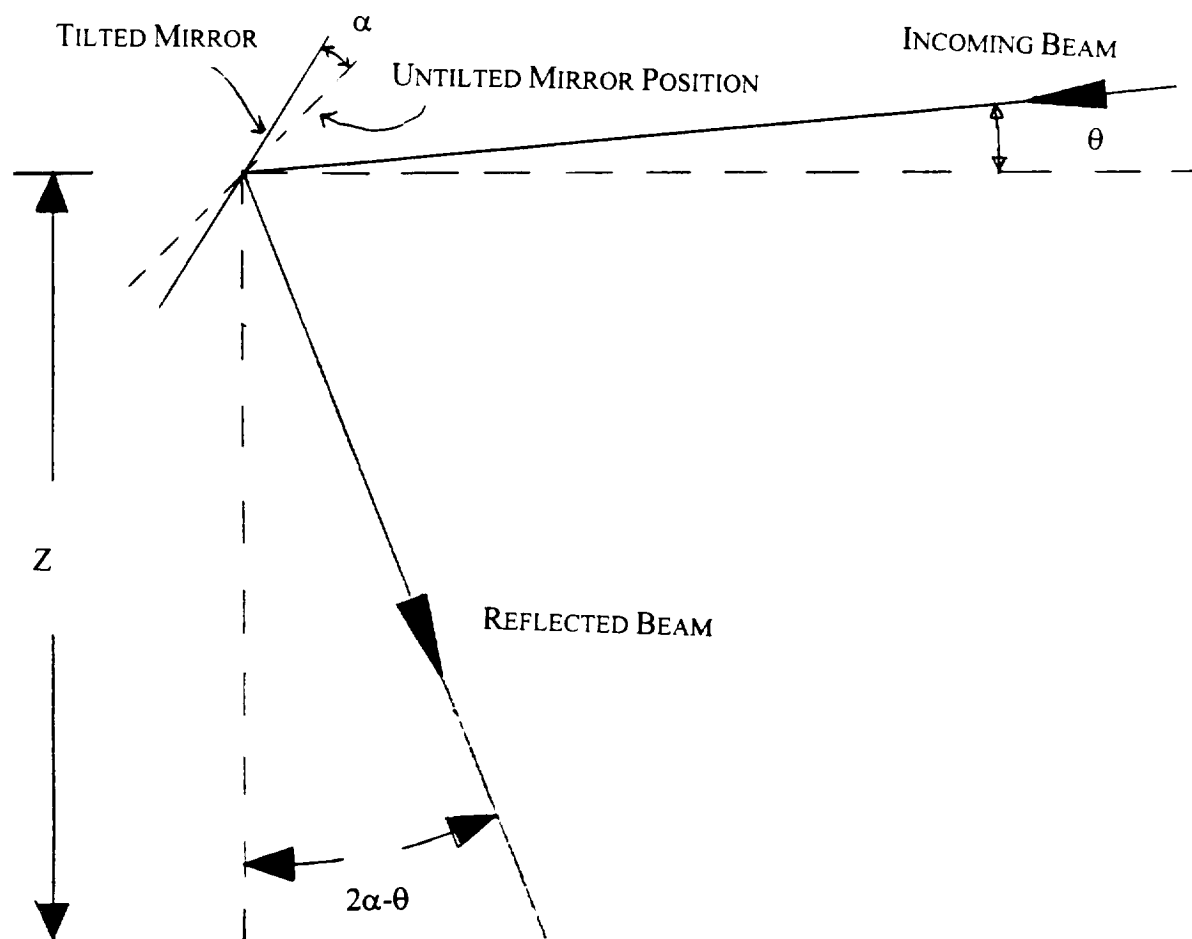
03/14/96 19:53

FIGURE 12b



$$\Delta\text{OPD} \cong \left(\frac{1}{\cos 2\alpha} - 1 \right) Z \cong 2\alpha^2 Z \quad (\text{small angles})$$

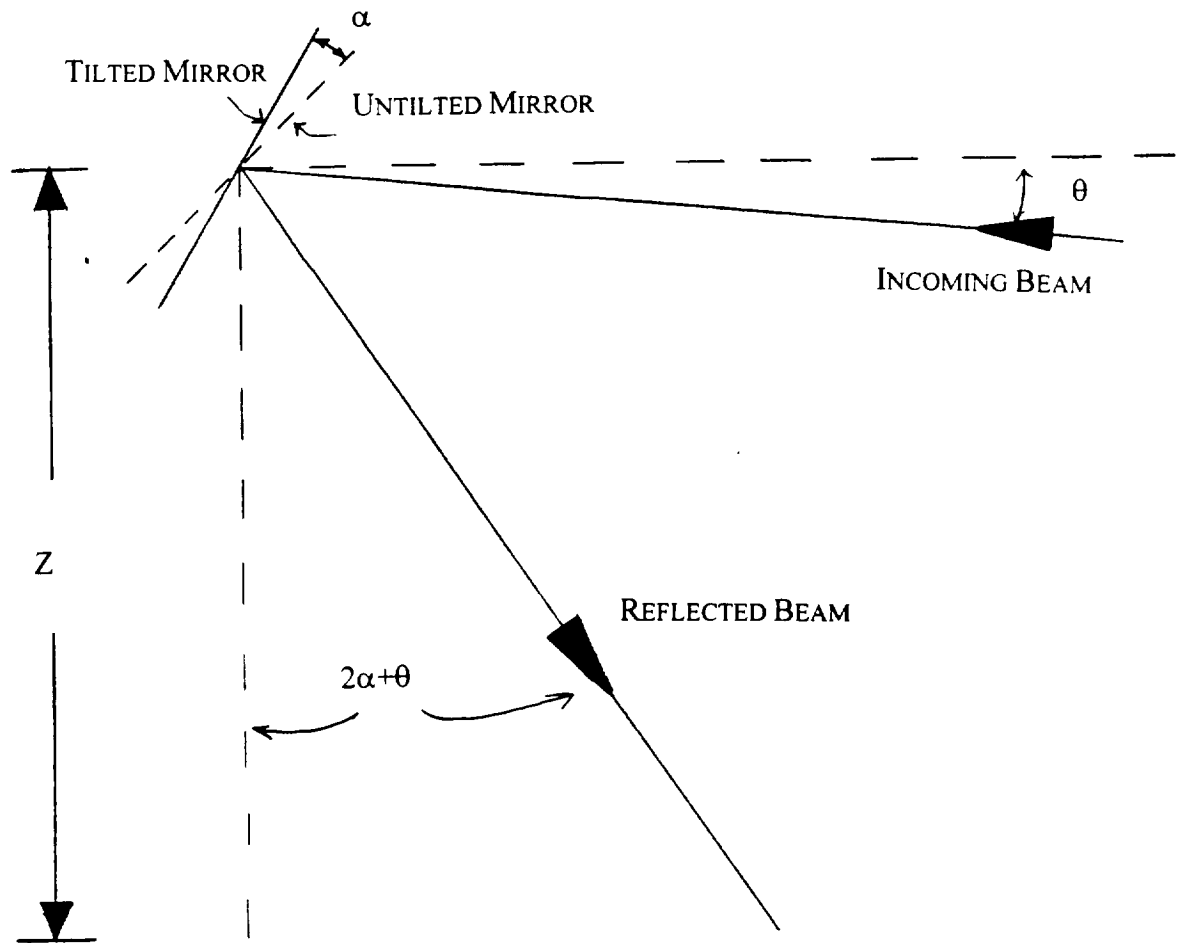
FIGURE 13



$$\Delta\text{OPD} \cong (2\alpha^2 - 2\alpha\theta)Z$$

(α, θ SMALL)

Figure 14

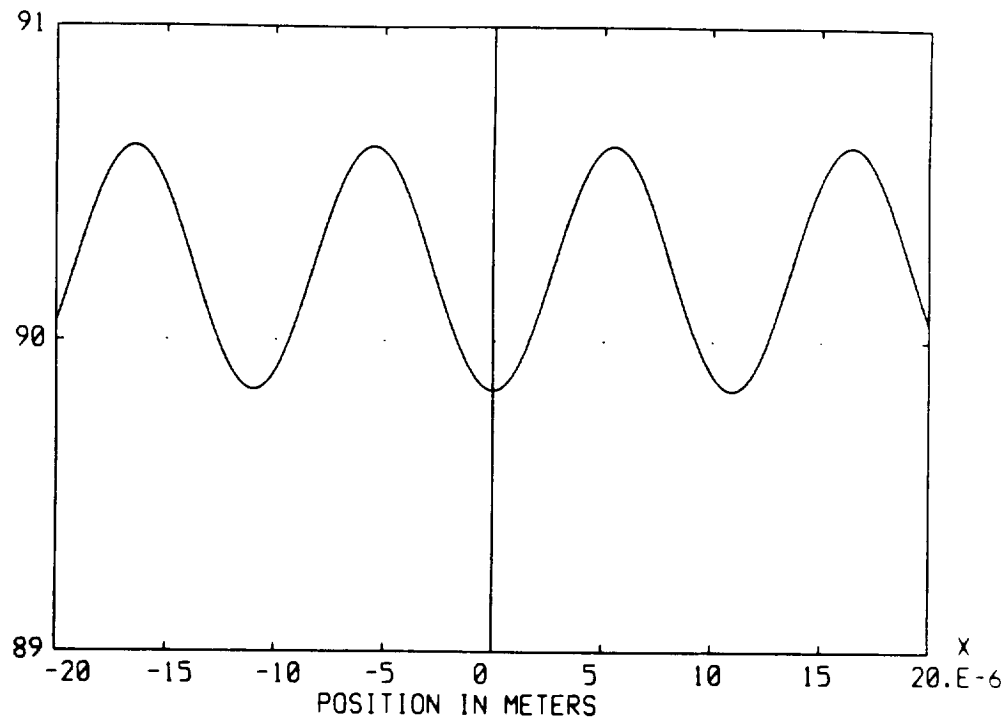


$$\Delta\text{OPD} \cong (2\alpha^2 + 2\alpha\theta) Z$$

(α, θ Small)

Figure 15

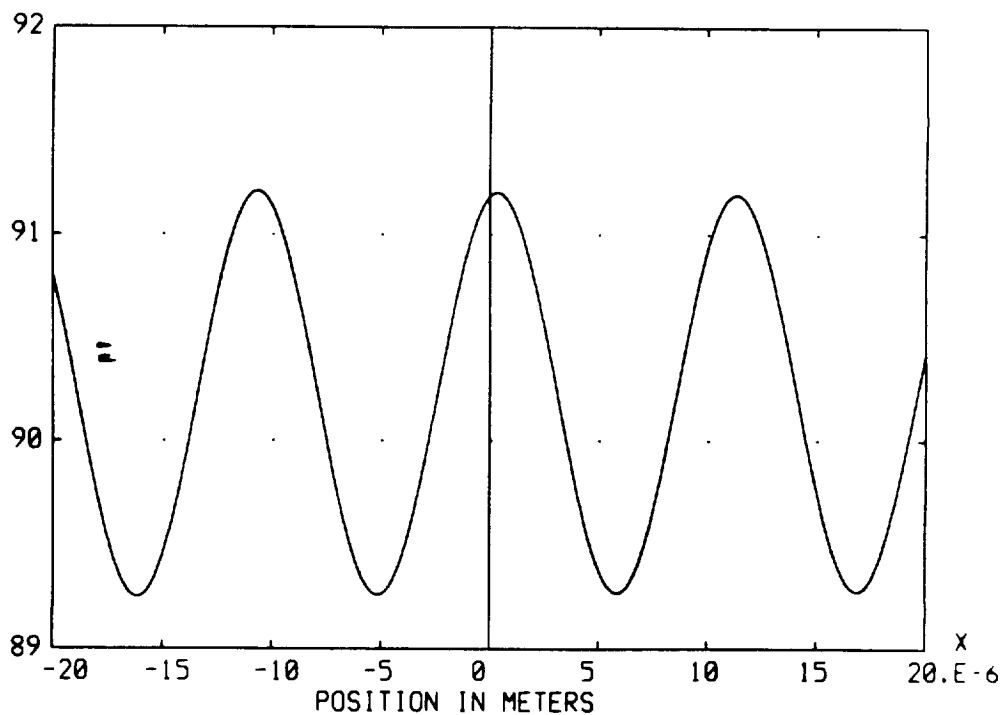
FRINGE PATTERN WITH DIFFRACTION EFFECT (VISIBILITY = .004)
 FLUX / UNIT-AREA



SOURCE OF 11 POINTS WITH AN ANGULAR SUBTENSE OF 100 MICRORADIANS
 SLIT WIDTH IS .933333 mm BASELINE IS 1 METERS WAVELENGTH IS

FIGURE 16a

FRINGE PATTERN WITH DIFFRACTION EFFECT (VISIBILITY = .011)
 FLUX / UNIT-AREA

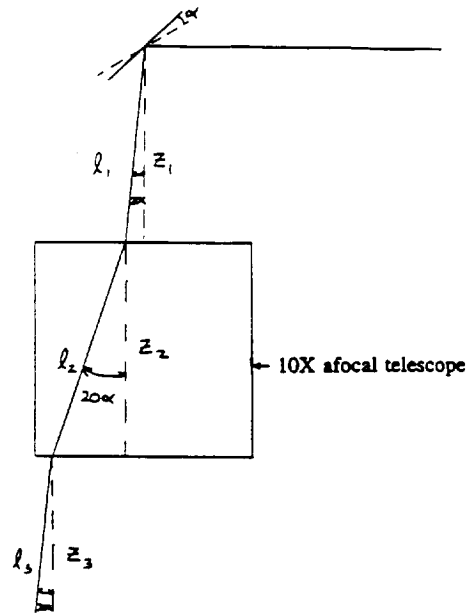


SOURCE OF 11 POINTS WITH AN ANGULAR SUBTENSE OF 100 MICRORADIANS
 SLIT WIDTH IS .933333 mm BASELINE IS 1 METERS WAVELENGTH IS

FIGURE 16b

INSTRUMENT TOLERANCE RESULTS

- MIRROR TILT



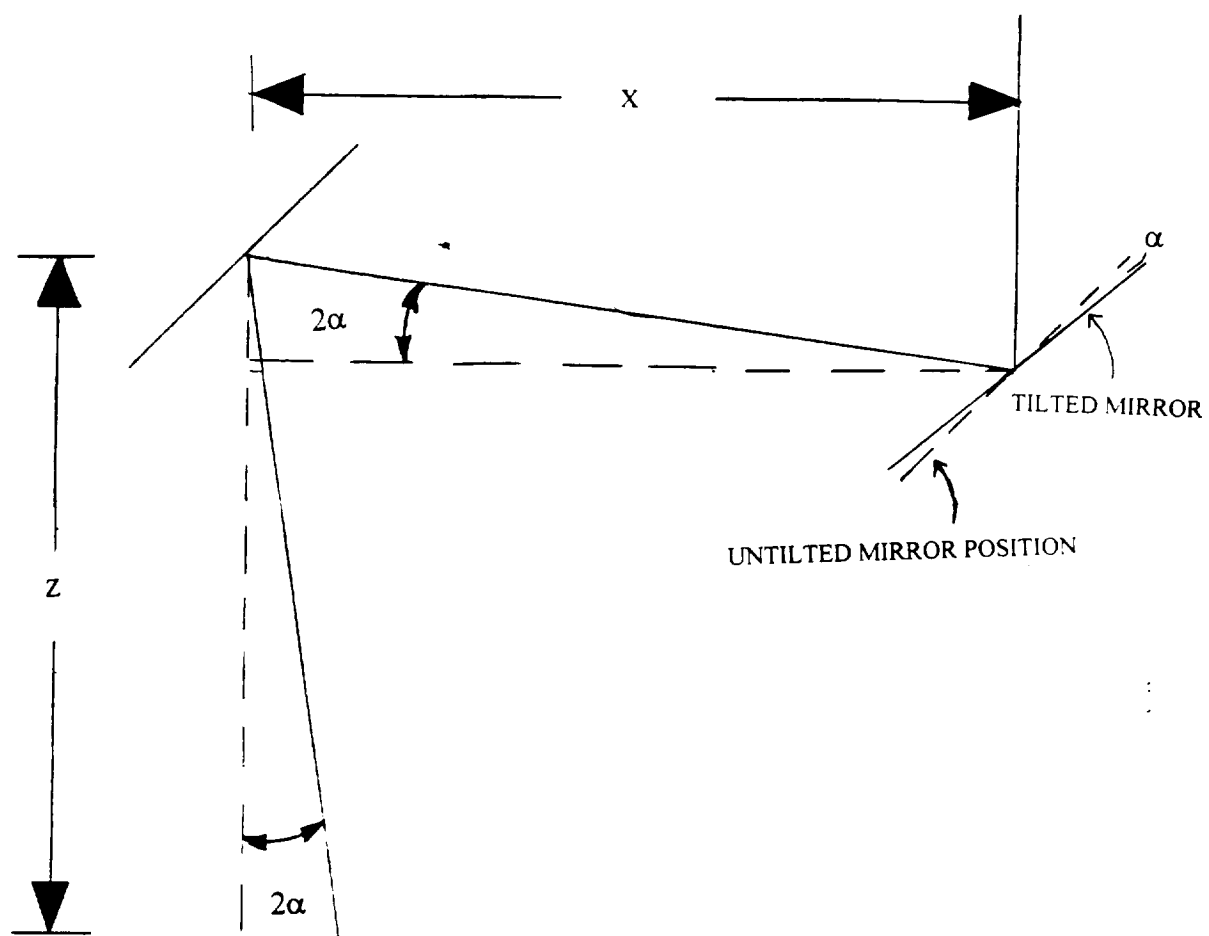
$$\Delta OPD_{TOTAL} = (l_1 - Z_1) + (l_2 - Z_2) + (l_3 - Z_3)$$

$$= Z_1 \left(\frac{1}{\cos(2\alpha)} - 1 \right) + Z_2 \left(\frac{1}{\cos(20\alpha)} - 1 \right) + Z_3 \left(\frac{1}{\cos(2\alpha)} - 1 \right)$$

AFOCAL EFFECT ~100X PER UNIT LENGTH

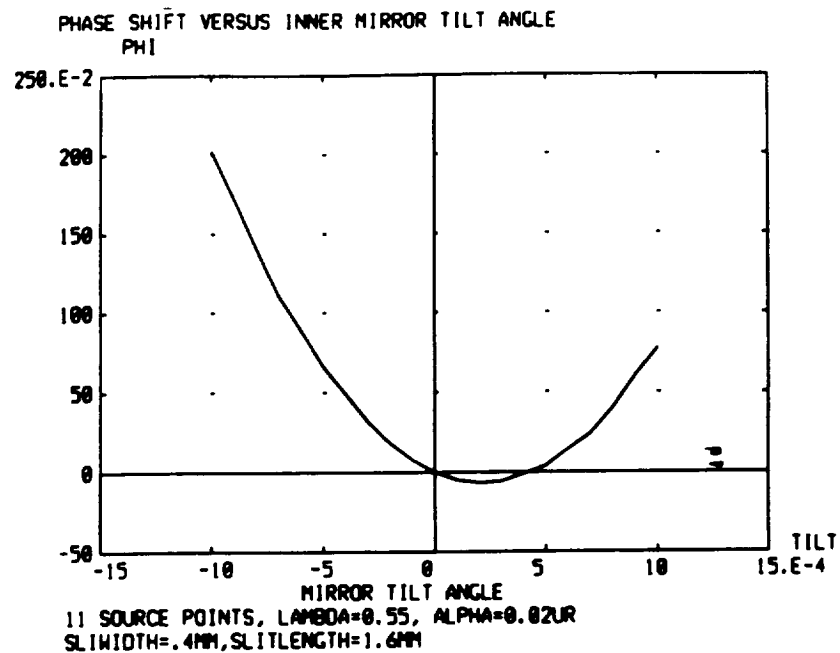
$$\frac{1}{\cos(2\alpha)} - 1 \approx 2\alpha^2 \quad \frac{1}{\cos(20\alpha)} - 1 \approx 200\alpha^2$$

FIGURE 17



$$\Delta\text{OPD} \approx 2\alpha^2 x + 2\alpha^2 z$$

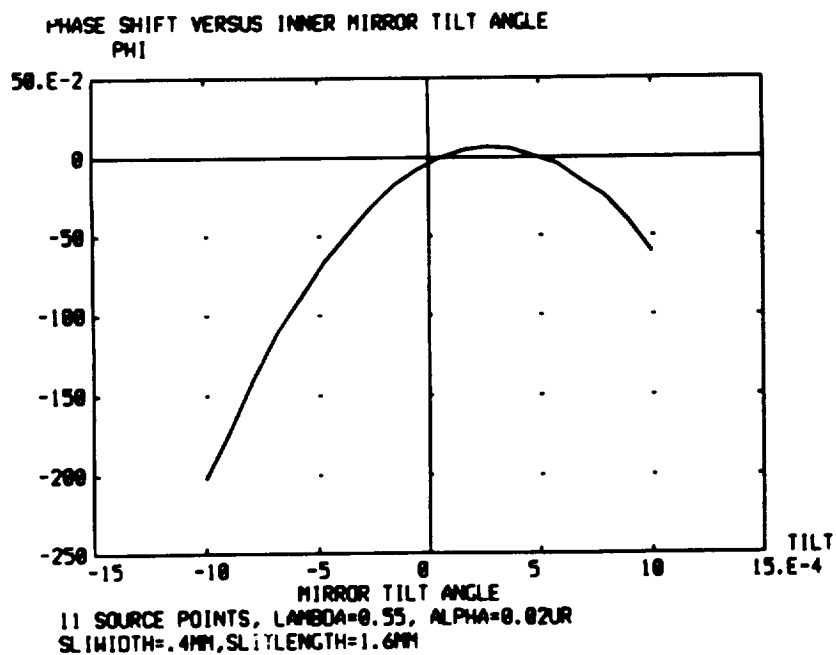
FIGURE 18



ASAP v4.0

03/20/96 23:32

FIGURE 19a



ASAP v4.0

03/16/96 17:33

FIGURE 19b

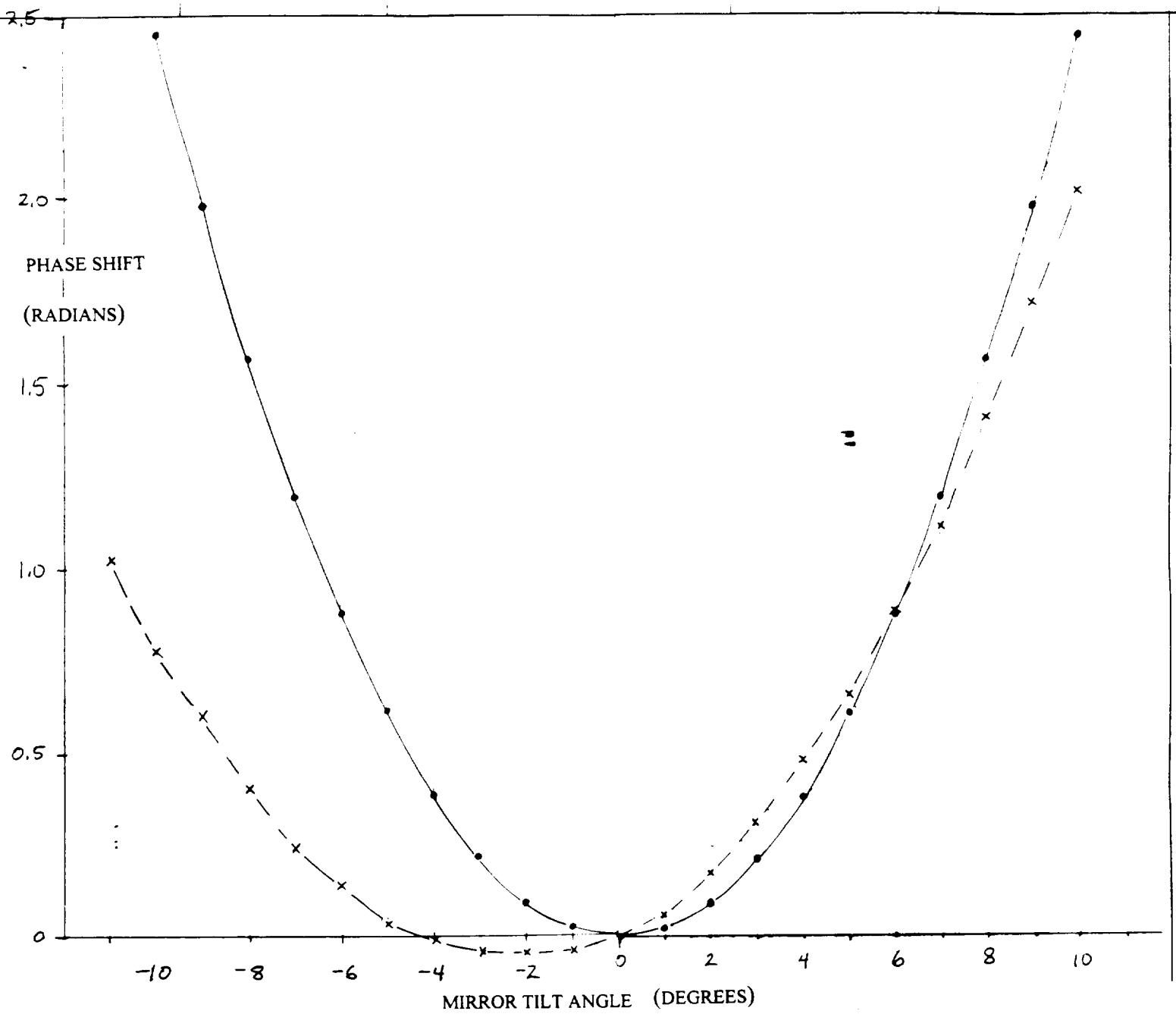
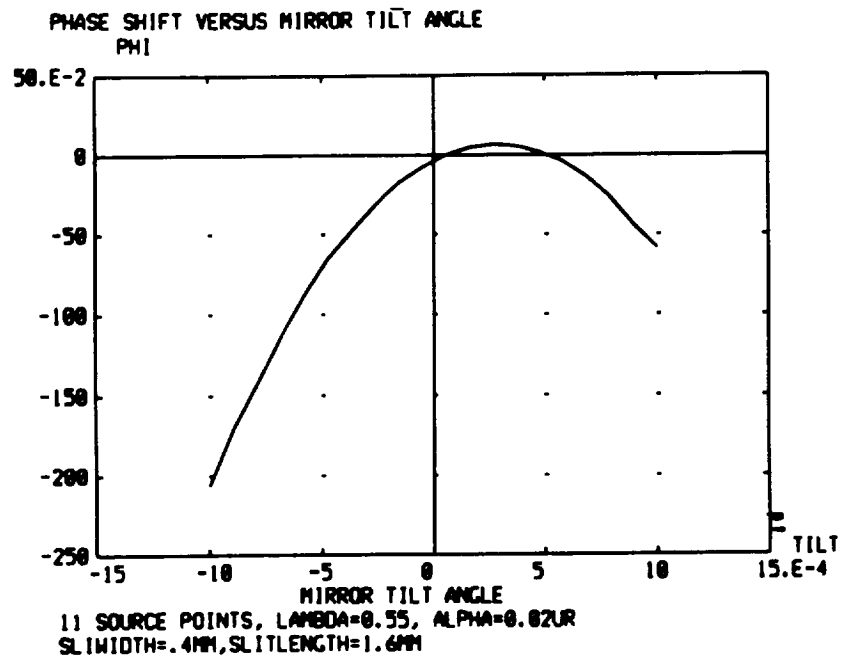


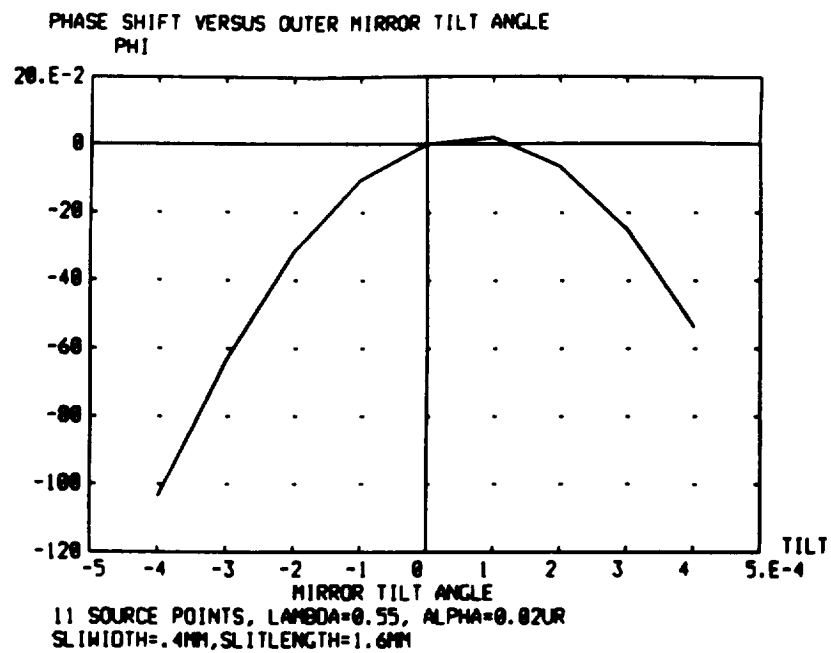
FIGURE 20



ASAP v4.0

03/12/96 15:34

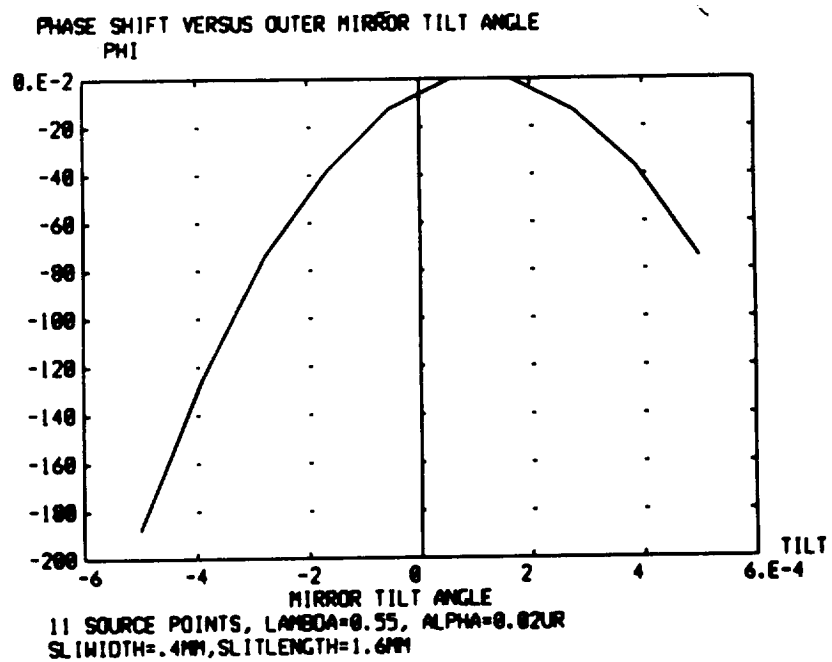
FIGURE 21a



ASAP v4.0

03/18/96 14:07

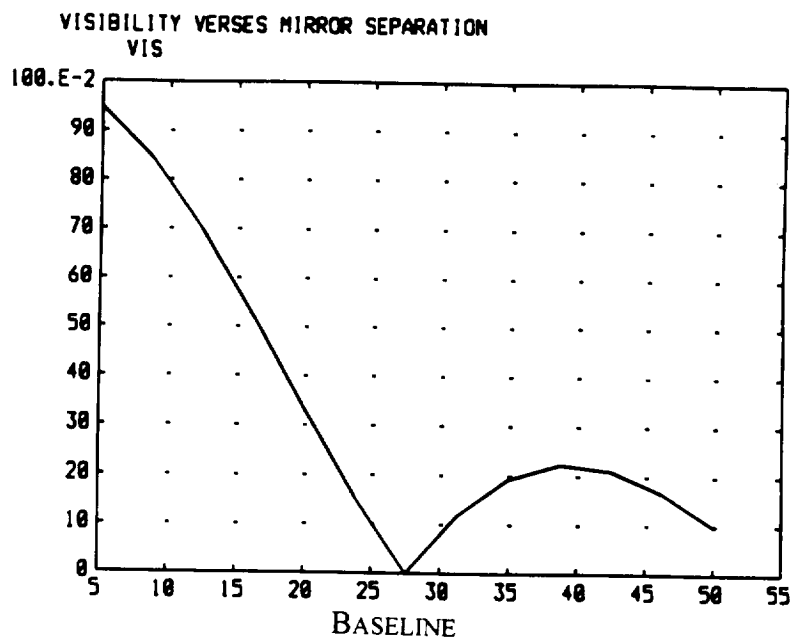
FIGURE 21b



ASAP v4.0

03/18/96 15:45

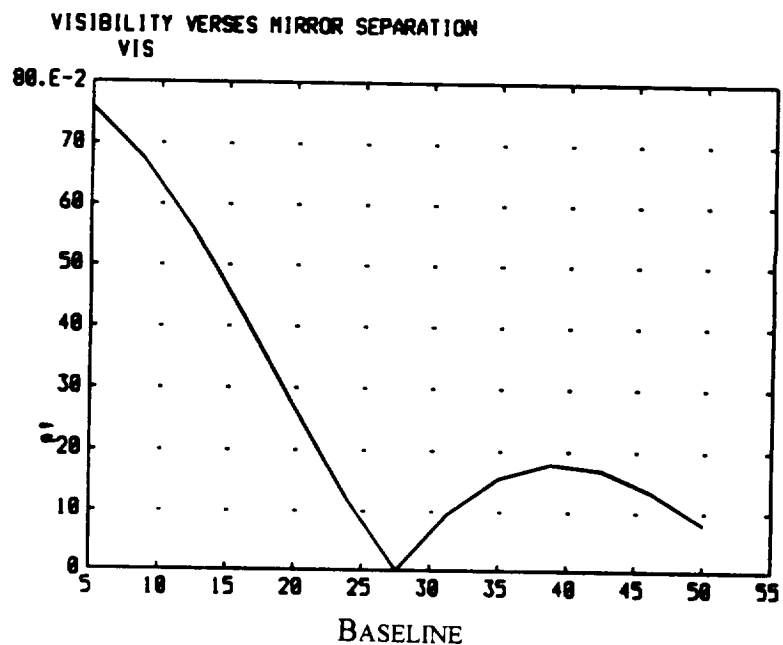
FIGURE 21c



MIRROR SEPARATION
11 SOURCE POINTS, $\lambda = 0.55$, $\alpha = 0.02$ UR
SLITWIDTH=0.4MM, SLITLENGTH=1.6MM
ASAP V4.0

09/03/95 21:58

FIGURE 22a



MIRROR SEPARATION
11 SOURCE POINTS, $\lambda = 0.55$, $\alpha = 0.02$ UR
SLITWIDTH=0.4MM, SLITLENGTH=1.6MM
ASAP V4.0

09/02/95 20:15

FIGURE 22b

VISIBILITY VERSES MIRROR SEPARATION
PHI

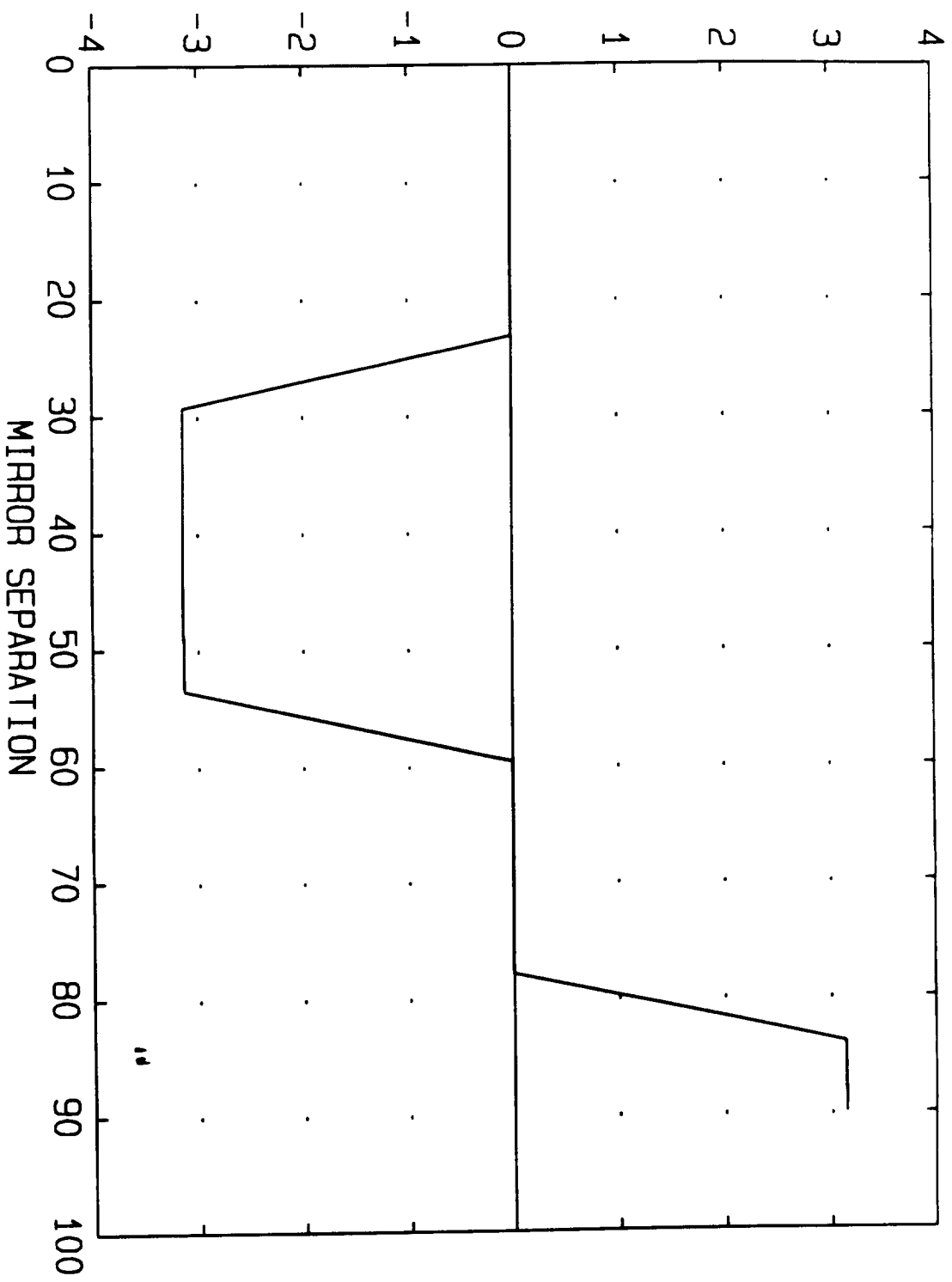


FIGURE 23a

VISIBILITY VERSES MIRROR SEPARATION PHI

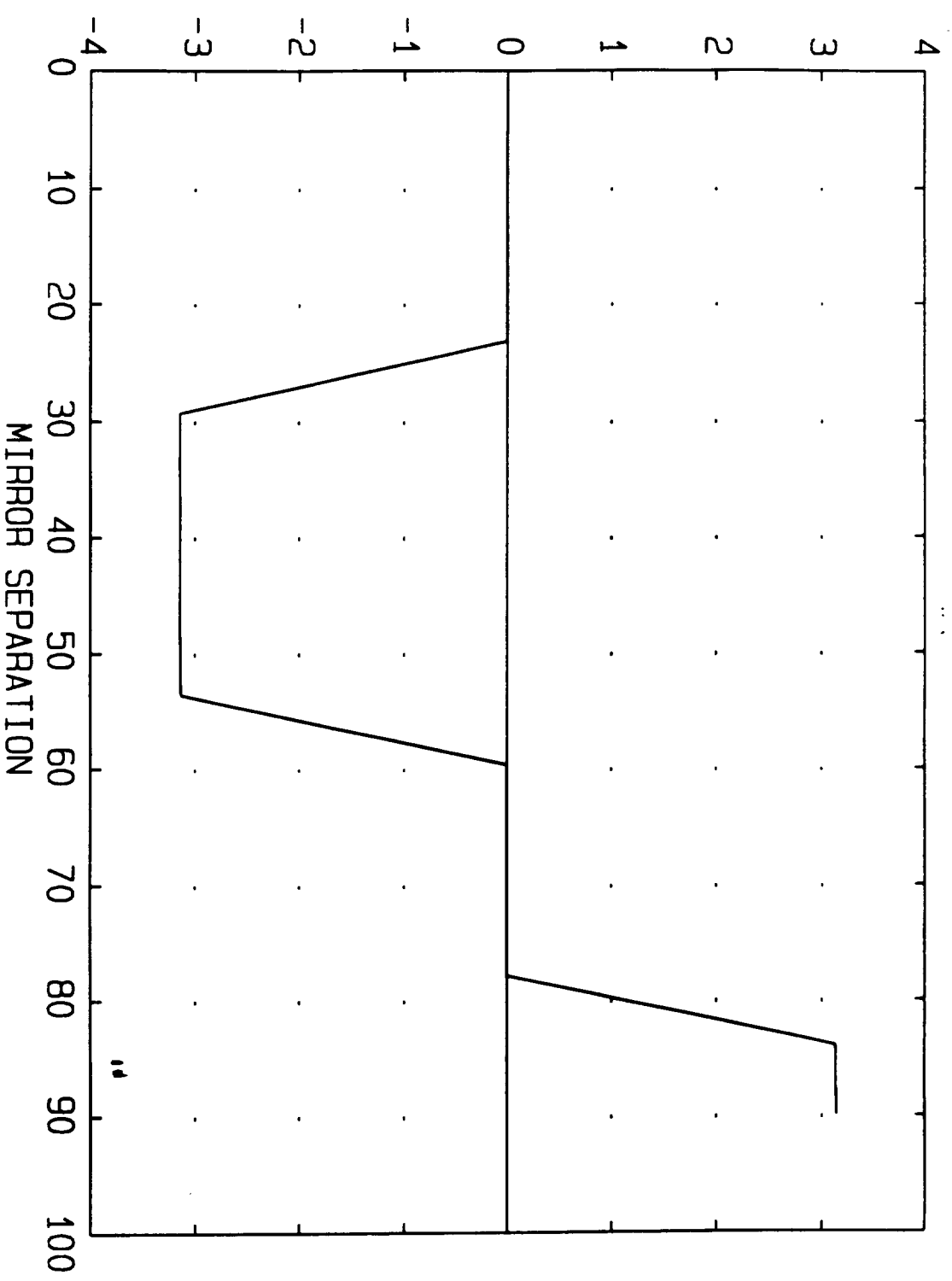


FIGURE 23b



VISIBILITY VERSES MIRROR SEPARATION PHI

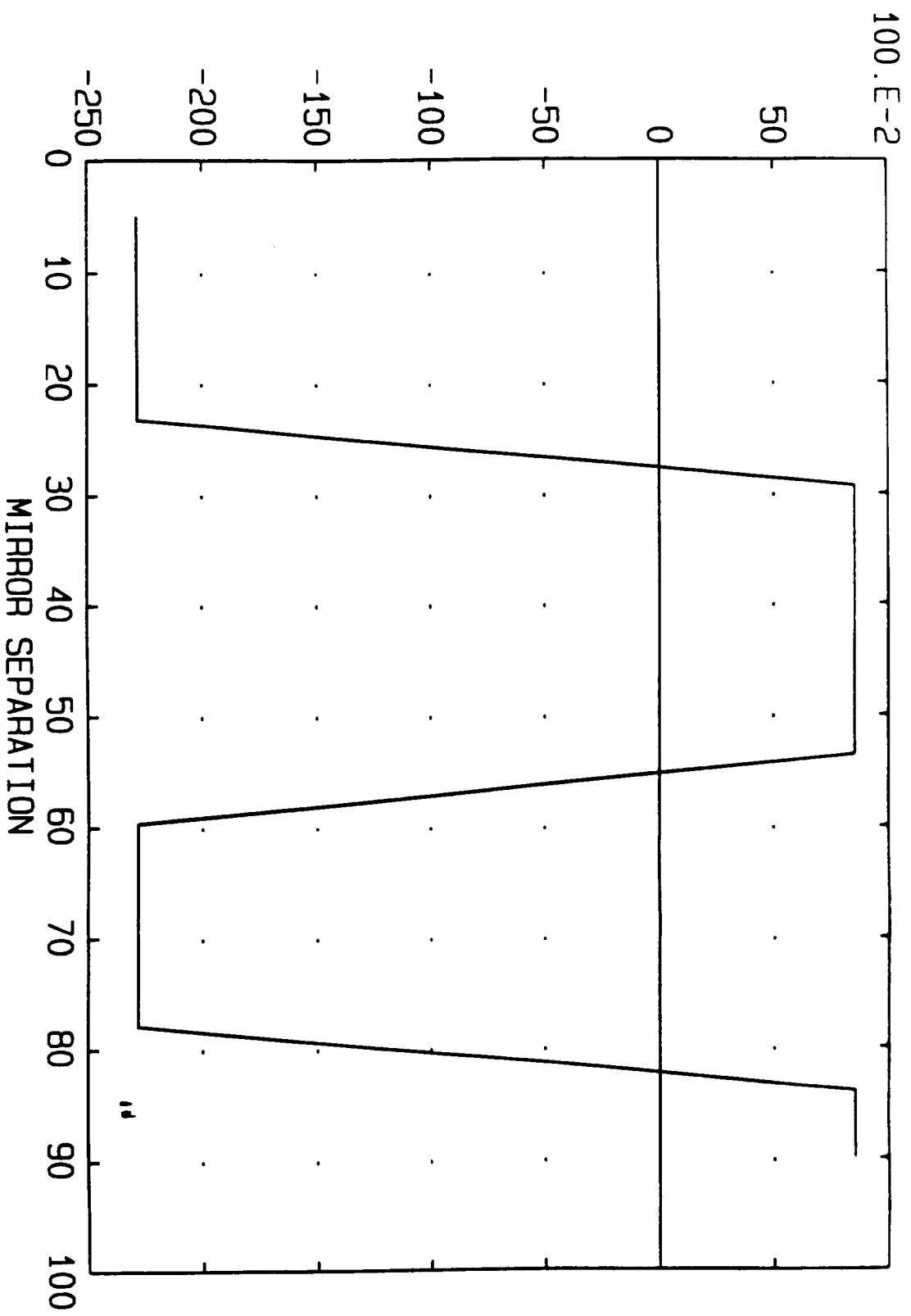


FIGURE 23c

VISIBILITY VERSES MIRROR SEPARATION PHI

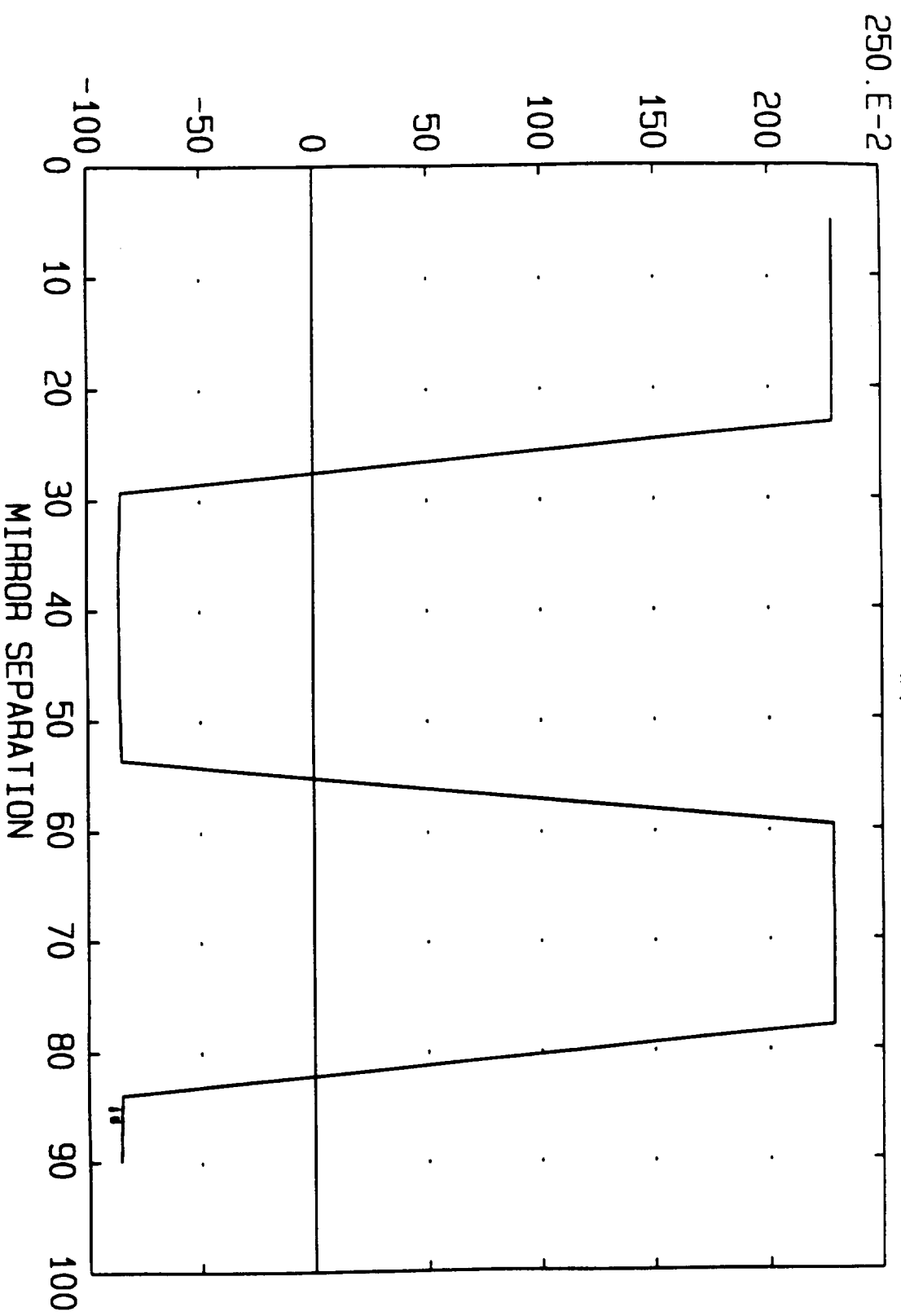
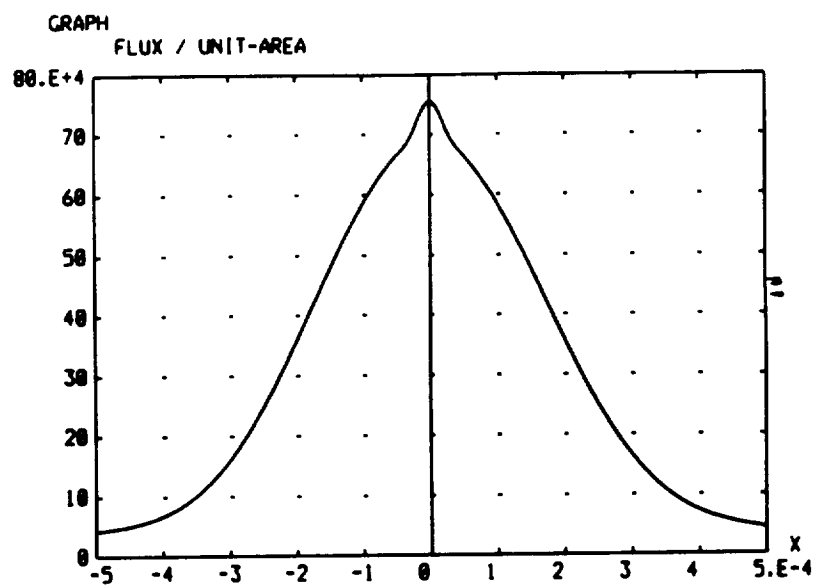


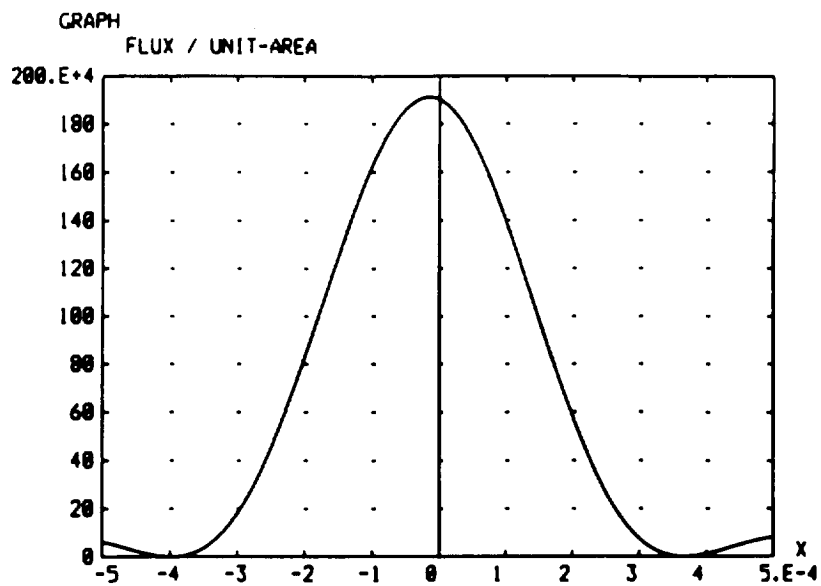
FIGURE 23d



ASAP v4.8

03/04/96 09:32 ASAP

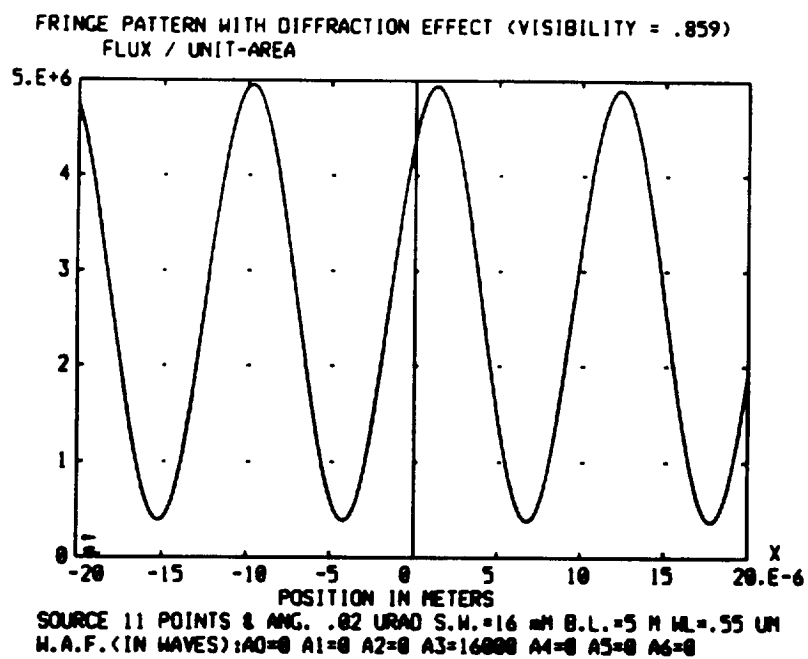
FIGURE 24a



ASAP v4.0

03/04/96 09:38 ASAP v4.0

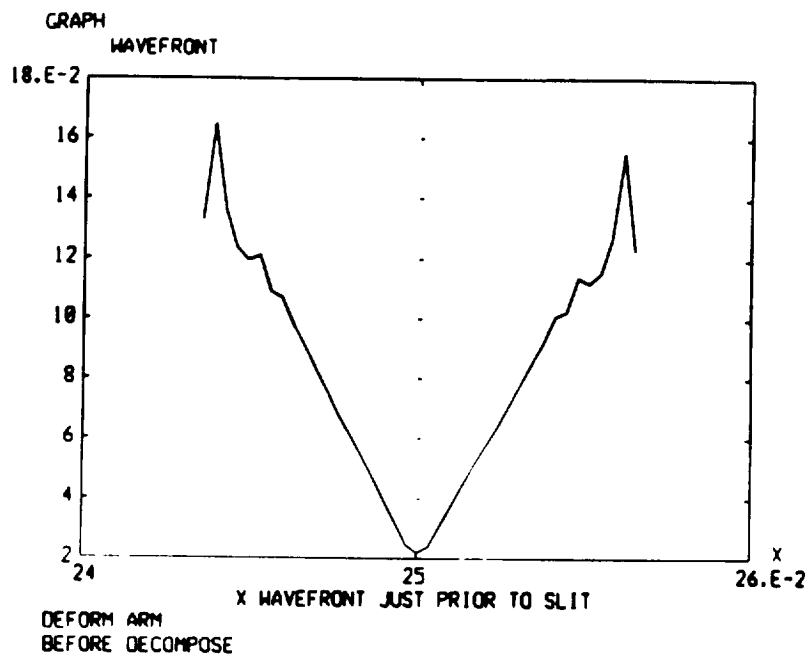
FIGURE 24b



ASAP v4.0

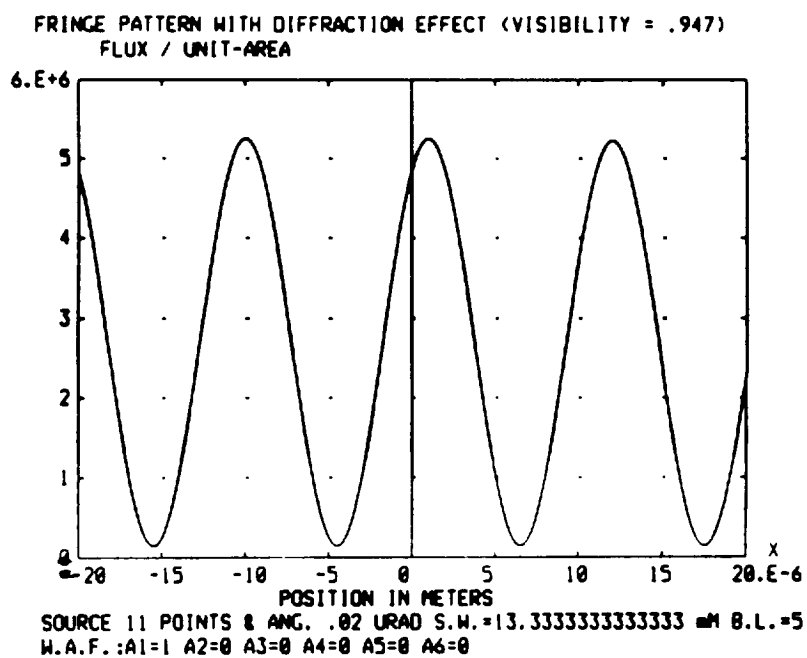
03/04/96 09:51 ASAP v4.0

FIGURE 24c



ASAP v4.0

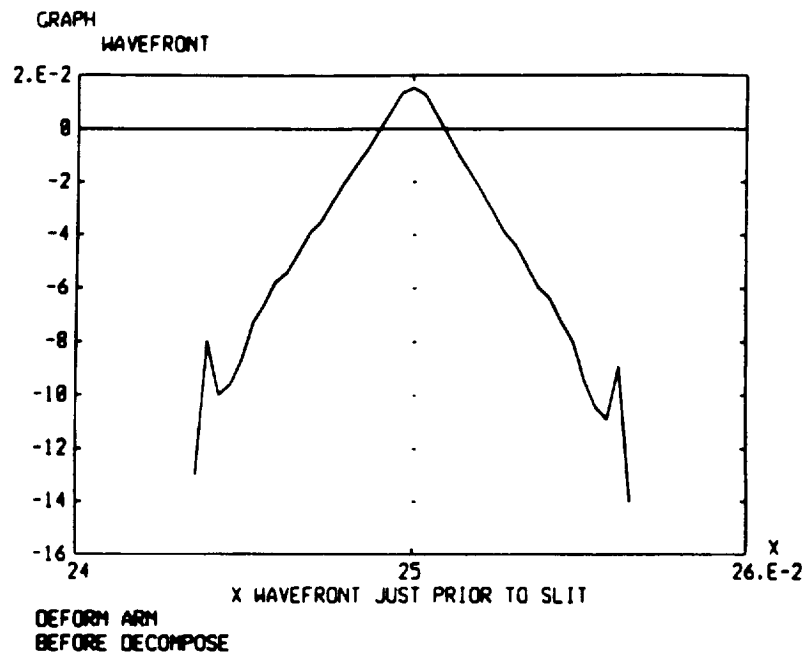
03/24/96 04:07 ASAP v4.0



ASAP v4.0

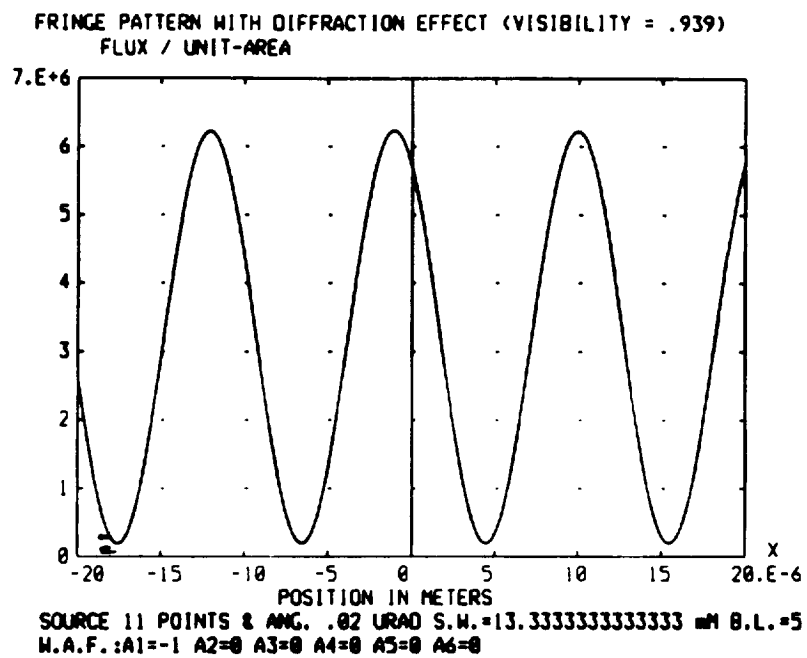
03/24/96 04:48

FIGURE 25a



ASAP v4.0

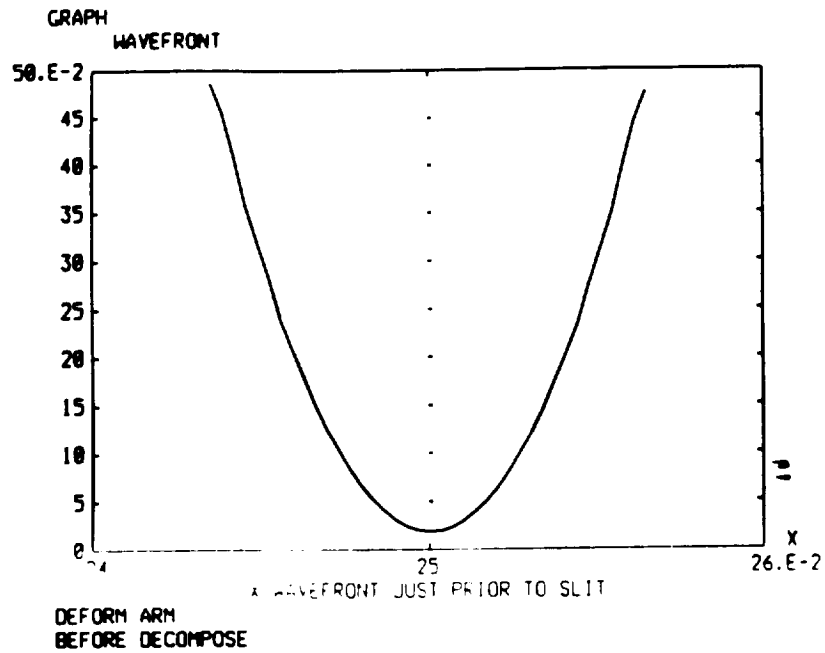
03/24/96 05:30



ASAP v4.0

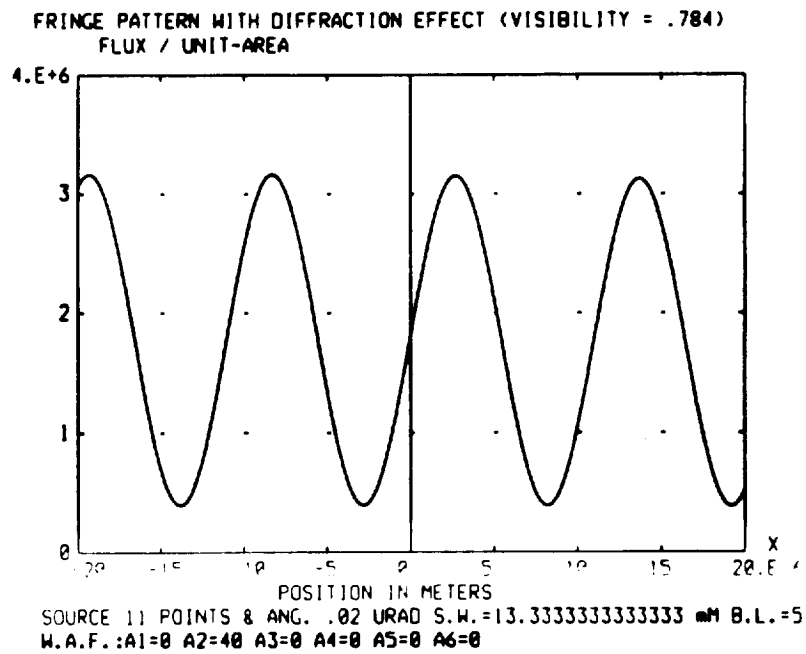
03/24/96 06:11

FIGURE 25b



ASAP v4.0

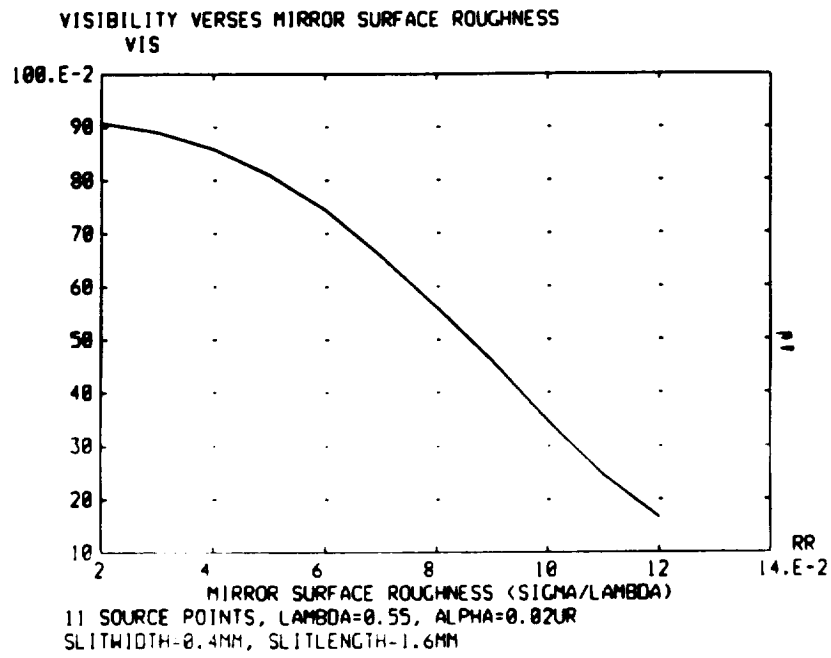
03/24/96 08:17



ASAP v4.0

03/24/96 08:57

FIGURE 25c



ASAP v4.0

03/26/96 10:11

FIGURE 26a

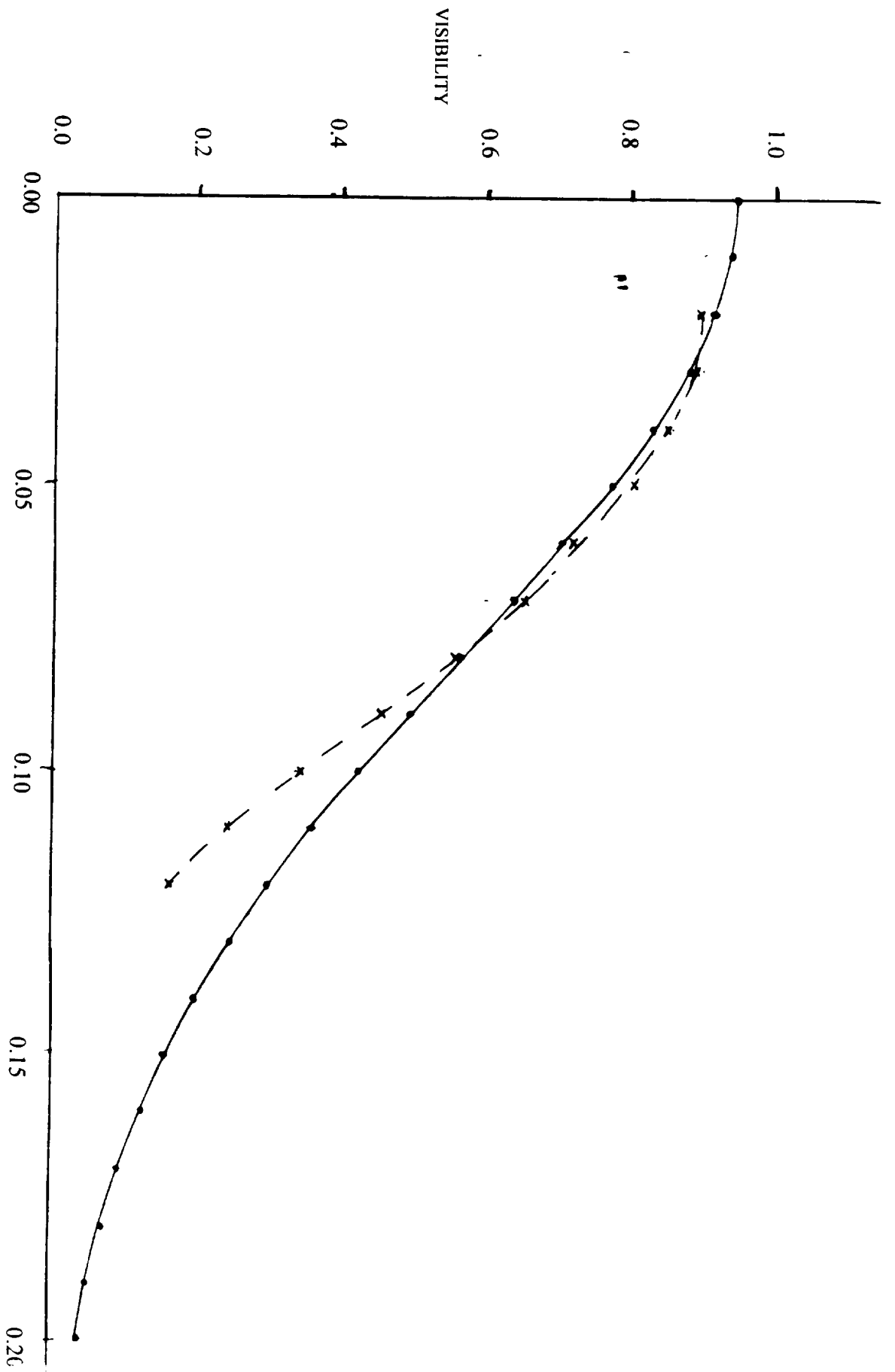


FIGURE 26b
SURFACE ROUGHNESS (σ/λ)



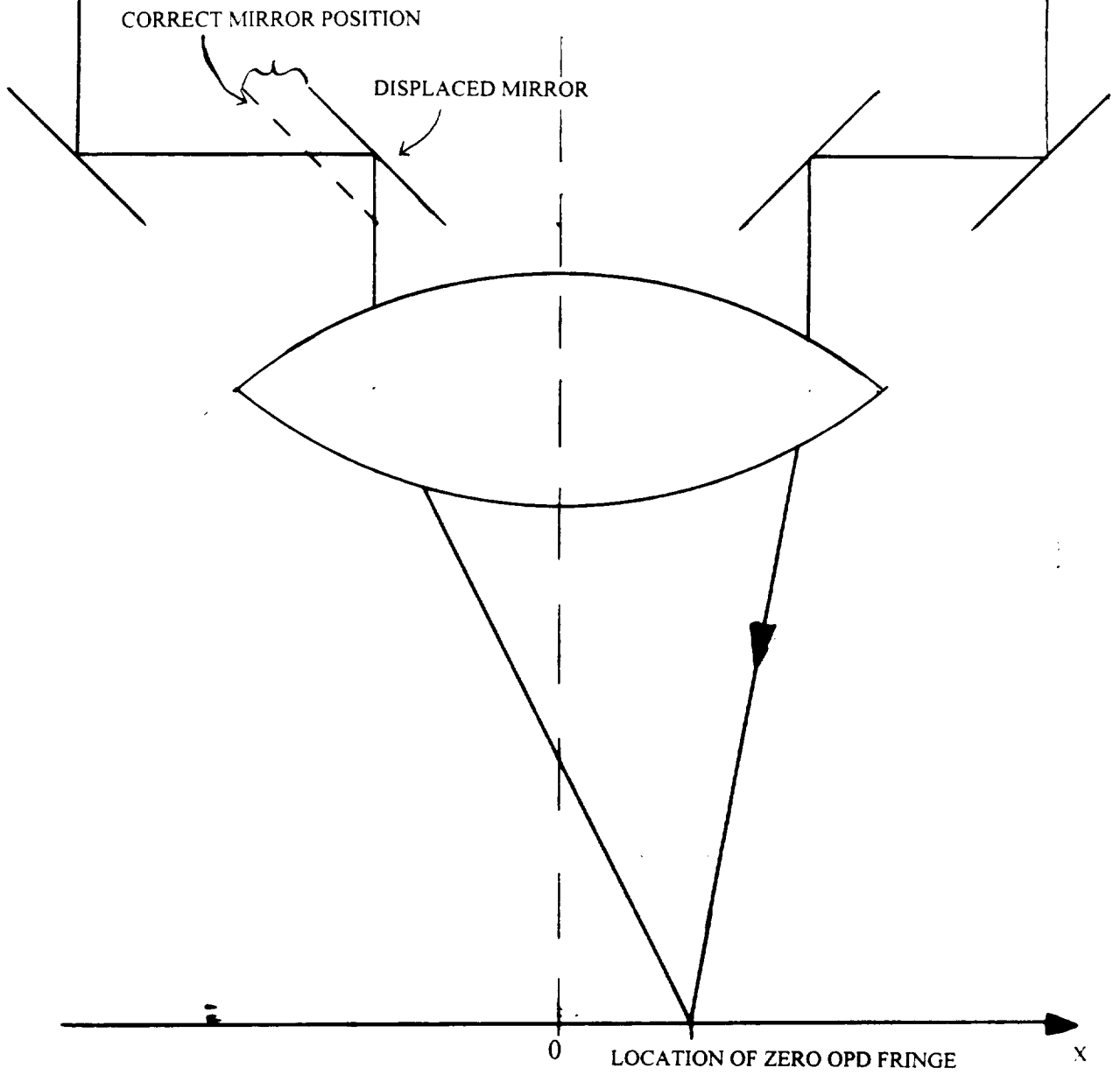


FIGURE 27

FRINGE PATTERN WITH DIFFRACTION EFFECT (VISIBILITY = .947) FLUX / UNIT-AREA

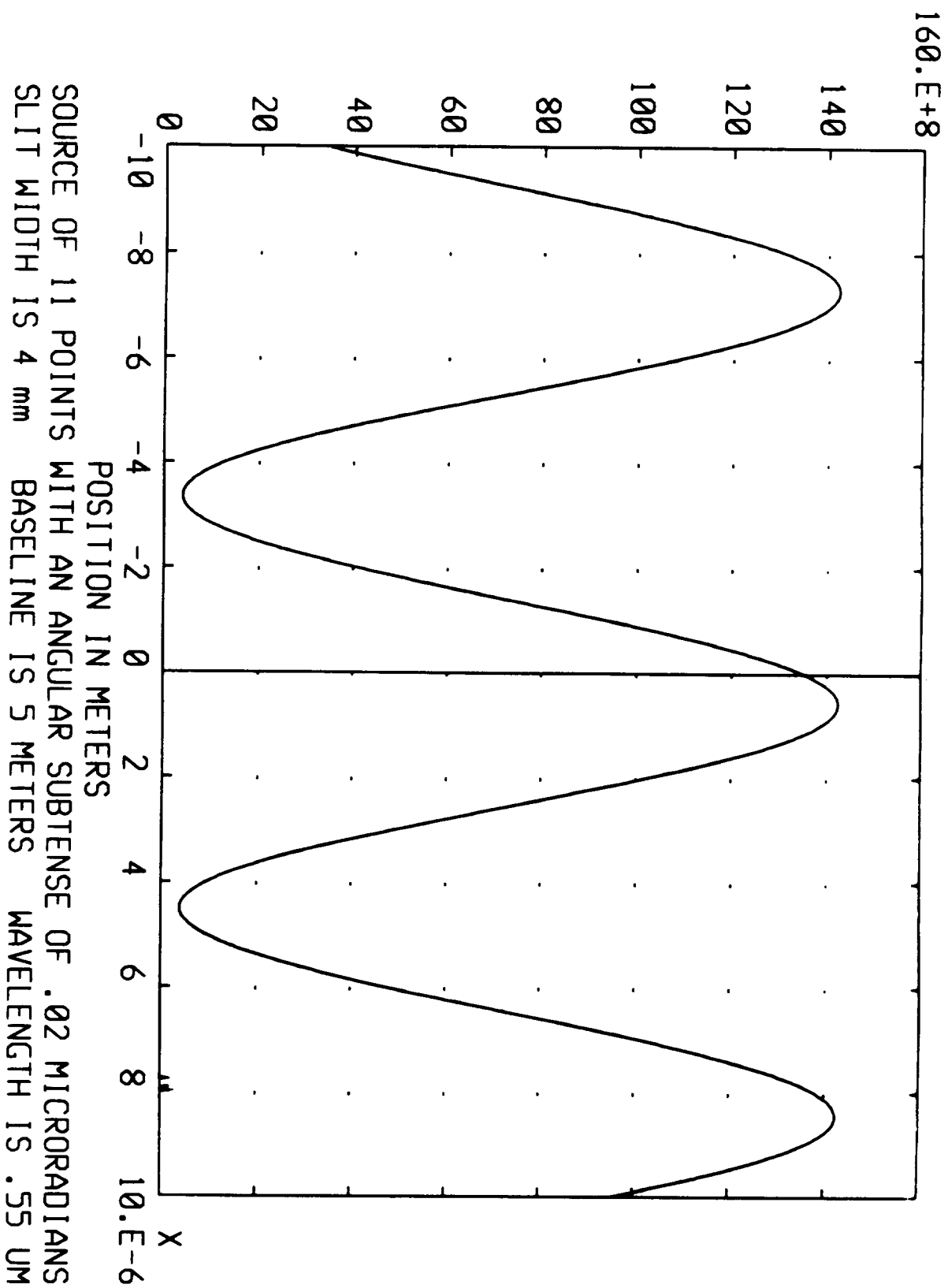


FIGURE 28



VISIBILITY VERSES MIRROR SEPARATION
PHI

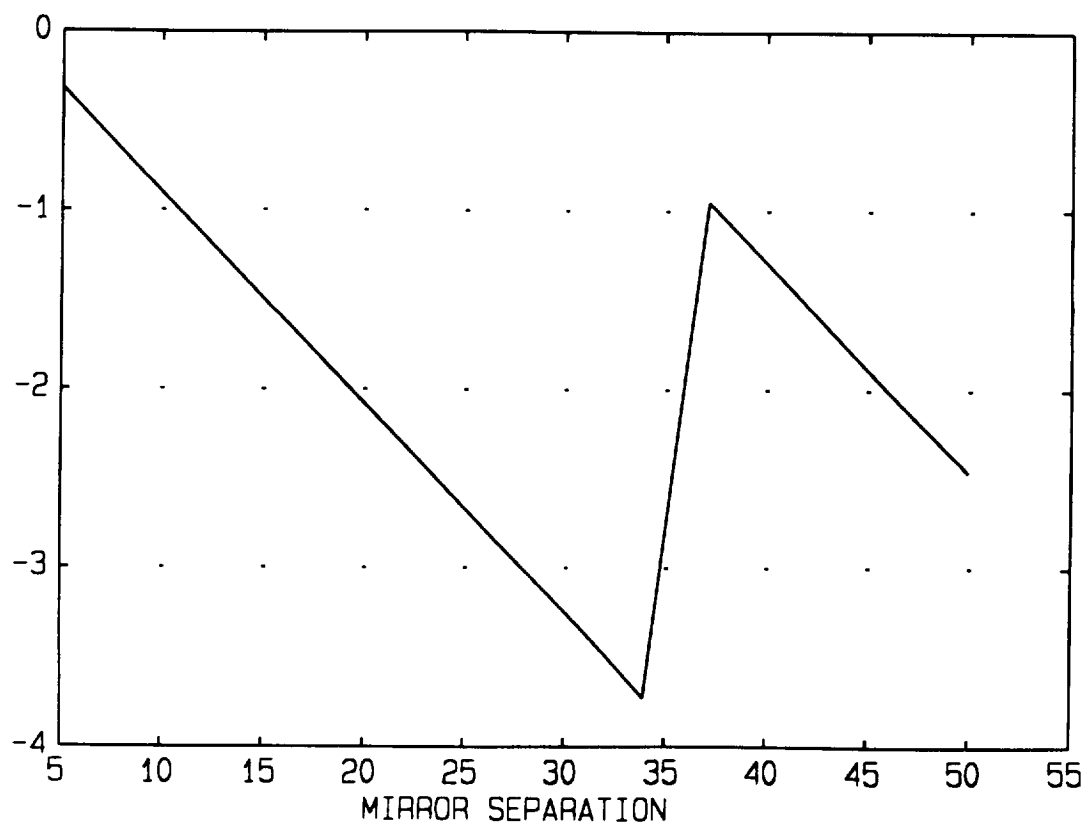


FIGURE 29a

VISIBILITY VERSES MIRROR SEPARATION
PHI

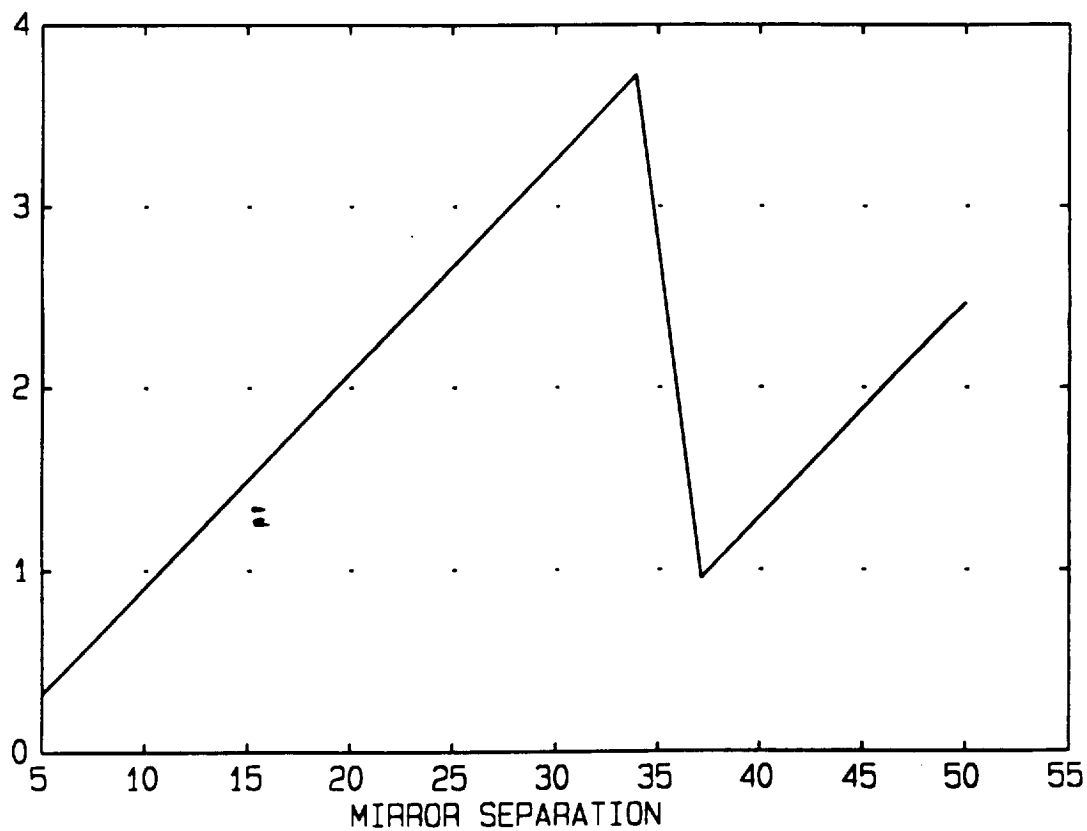


FIGURE 29b

FRINGE PATTERN WITH DIFFRACTION EFFECT (VISIBILITY = .998)
 FLUX / UNIT-AREA

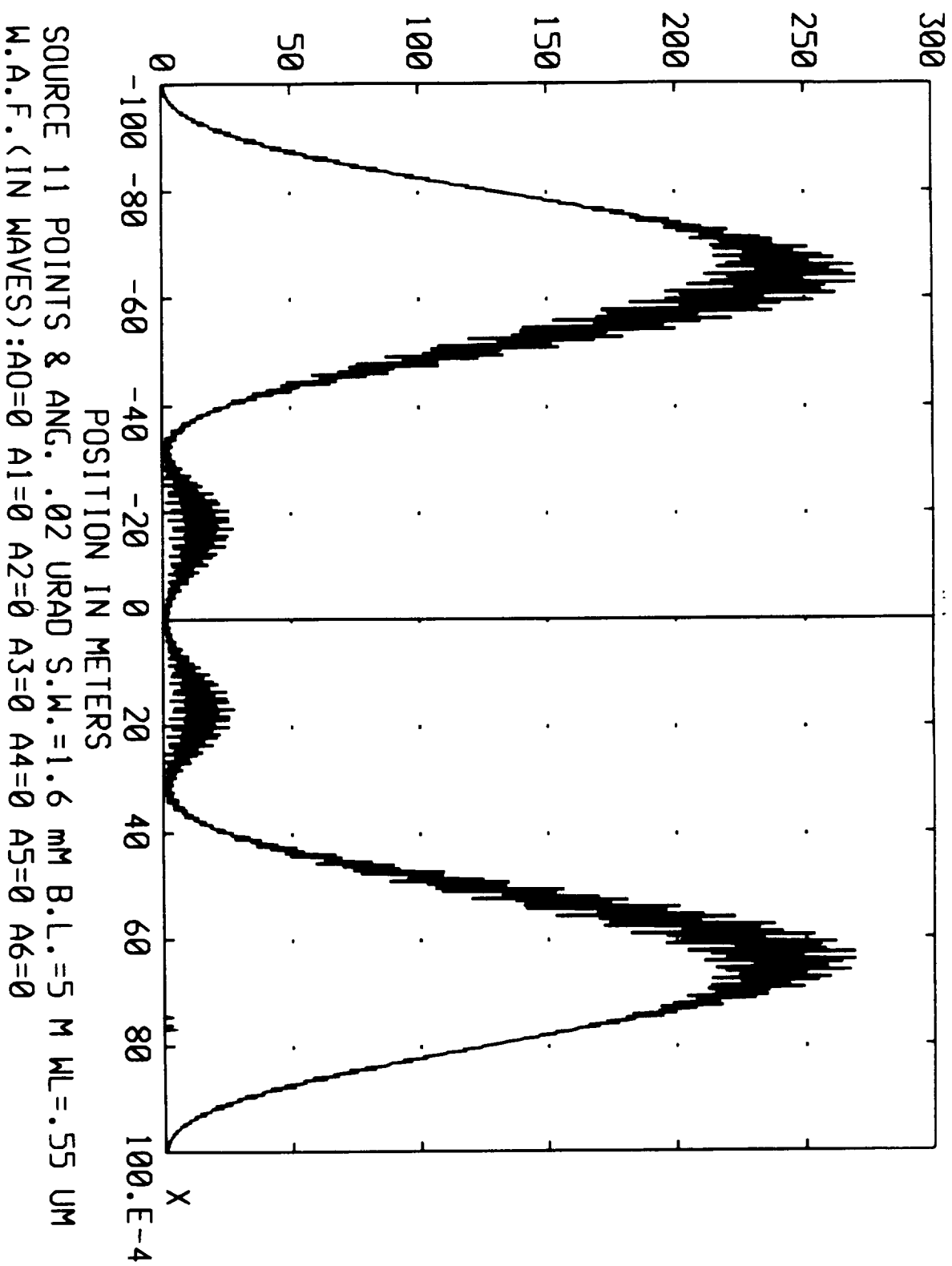
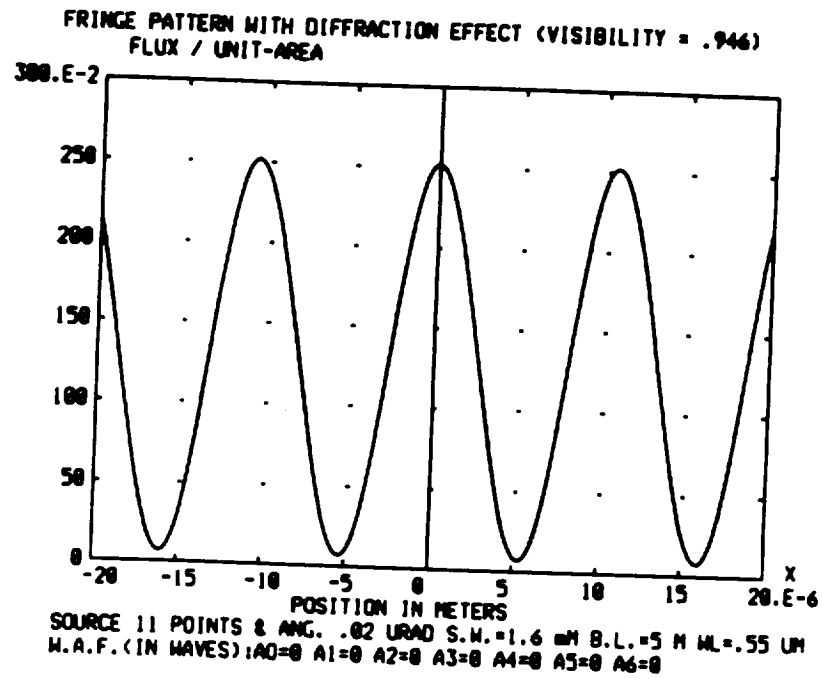


FIGURE 30a

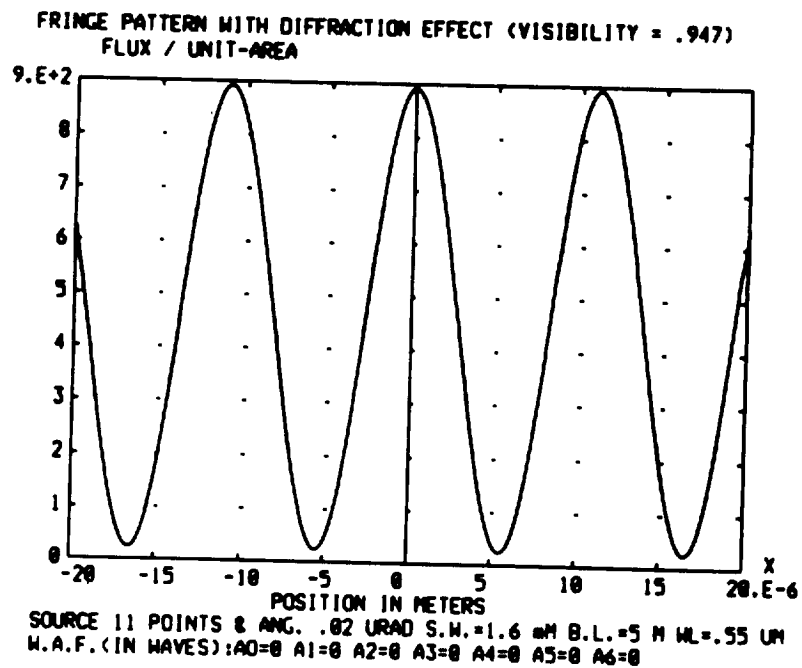




① ASAP v4.8

02/23/96 13:33

FIGURE 30b

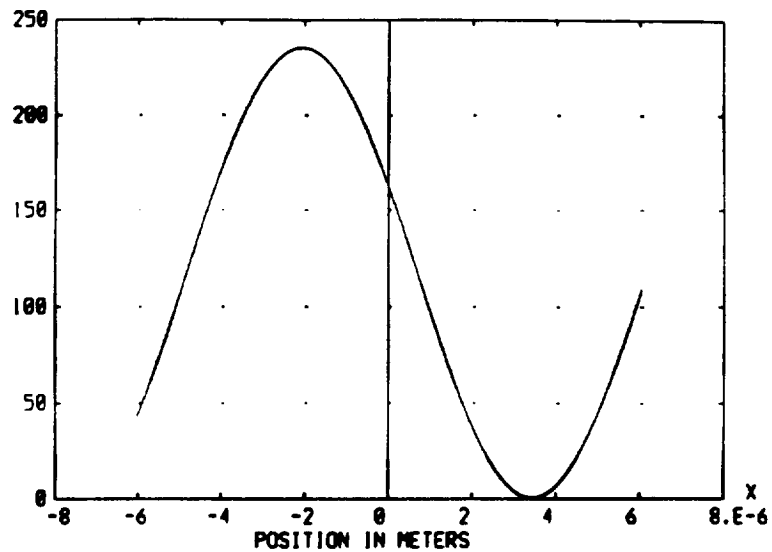


① ASAP v4.8

02/21/96 22:34

FIGURE 30c

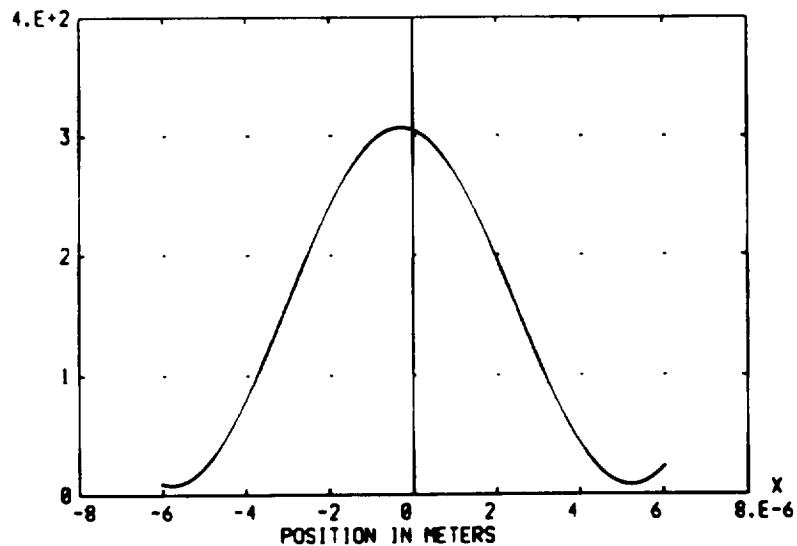
FRINGE PATTERN ($\Phi = -1.188292565764$) (VISIBILITY = .995)
 FLUX / UNIT-AREA



SOURCE OF 11 POINTS WITH AN ANGULAR SUBTENSE OF .0002 MICRORADIA
 SLIT WIDTH IS 1 mm BASELINE IS 5 METERS WAVELENGTH IS .55 UM

FIGURE 31a

FRINGE PATTERN ($\Phi = -.16291116321746$) (VISIBILITY = .948)
 FLUX / UNIT-AREA



SOURCE OF 11 POINTS WITH AN ANGULAR SUBTENSE OF .0002 MICRORADIA
 SLIT WIDTH IS 1 mm BASELINE IS 5 METERS WAVELENGTH IS .55 UM

FIGURE 31b

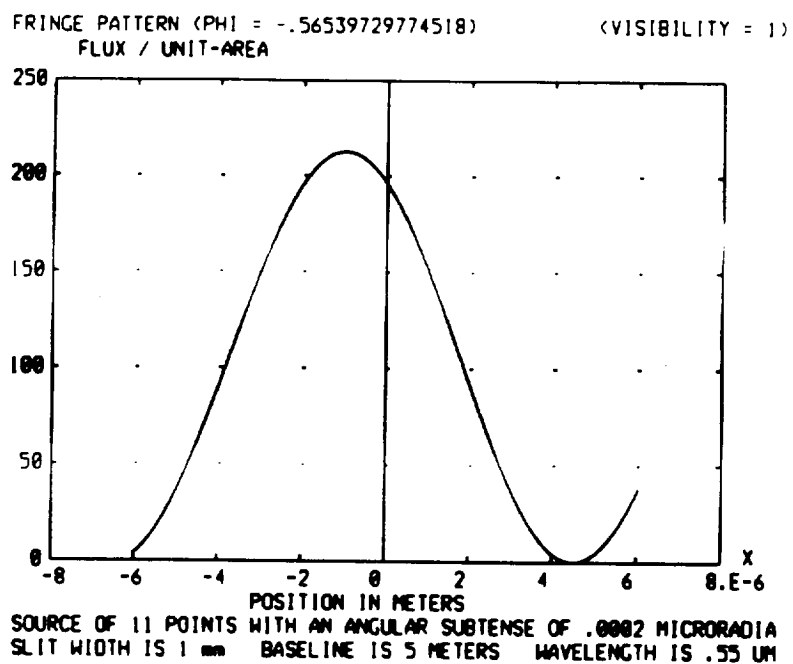


FIGURE 31c

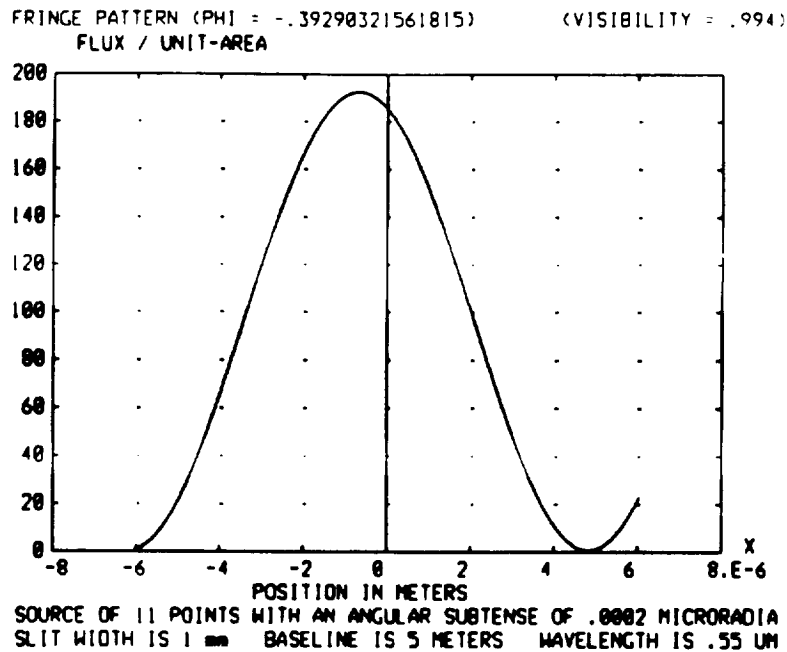


FIGURE 31d